

Immobilized cellulose nanospheres in lateral flow immunoassay enable rapid nucleocapsid antigen-based diagnosis of SARS-CoV-2 from salivary samples

*Katariina Solin^{1,2}, Marco Beaumont³, Maryam Borghei¹, Hannes Orelma², Pascal Mertens⁴, and
Orlando J. Rojas^{1,5,*}*

¹Department of Bioproducts and Biosystems, School of Chemical Engineering, Aalto University,
Vuorimiehentie 1, FI-00076, Espoo, Finland

²VTT Technical Research Centre of Finland Ltd., Tietotie 4E, FI-02044 Espoo, Finland

³Department of Chemistry, Institute of Chemistry for Renewable Resources, University of
Natural Resources and Life Sciences Vienna (BOKU), Konrad-Lorenz-Straße 24, A-3430 Tulln,
Austria

⁴Coris BioConcept, Rue Jean Sonet 4A, B-5032 Gembloux, Belgium

⁵The Bioproducts Institute, Department of Chemical and Biological Engineering, Department of
Chemistry and Department of Wood Science, University of British Columbia, 2360 East Mall,
Vancouver, BC, V6T 1Z4 Canada

Keywords: Patterning; protein interactions; paper-based diagnostics; coronavirus antigen test;
immunoassay

ABSTRACT

Rapid and efficient diagnostic systems are essential in controlling the spread of viral pathogens and efficient patient management. The available technologies for low-cost viral antigen testing have several limitations, including lack of accuracy and sensitivity. Here, we develop sensitive antigen tests based on recently introduced, oppositely charged cellulose II nanoparticles (NPan and NPcat) that are effective in controlling surface protein interactions. Passivation against non-specific adsorption and augmented immobilization of sensing antibodies are achieved by adjusting the electrostatic charge of the nanoparticles. The interactions affecting the performance of the system are investigated by microgravimetry and confocal imaging. We further demonstrate SARS-CoV-2 nucleocapsid rapid sensing by saliva-wicking channels stencil-printed on flexible paper supports. Therein, NPcat inkjet printed on the channels elicit distinctive optical signals, visible after only a few minutes, allowing faster diagnosis compared to current microfluidic devices designed for saliva sampling.

INTRODUCTION

The COVID-19 pandemic has accelerated research aiming to develop diagnostic systems suitable for wide-scale screening of viral infections, enabling better control of virus transmission. Currently, the most common diagnostic methods for the severe acute respiratory syndrome coronavirus 2 (SARS-CoV-2) infection are reverse transcription-polymerase chain reaction (RT-PCR) and immunoassays¹. RT-PCR is a molecular biology method that amplifies RNA into larger and detectable amounts. The main advantage of RT-PCR is the high sensitivity, as only minor amounts of viral RNA are needed for amplification. However, PCR-based diagnosis requires

skilled personnel for sampling and analysis². This has been a demanding aspect that limits healthcare resources and capacity. This is especially relevant in areas or communities with limited diagnostic infrastructure. Besides, RT-PCR requires high-quality specimens containing appropriate amounts of intact viral RNA, therefore, relatively high false-negative rates have been reported due to the variation of SARS-CoV-2 loads in the clinical samples and spoliation during transport and storage².

Immunoassays are also instrumental in SARS-CoV-2 diagnosis, especially because they allow rapid point-of-care (POC) testing. Immunoassays utilize highly specific antibody-antigen interactions and tracers, such as specific molecules or polymers, to detect immune proteins from the sample. For example, antigen and antibody interactions open opportunities for portable, easy-to-use lateral flow assays (LFAs). Indeed, many reports describe the development of LFAs for SARS-CoV-2 testing³⁻⁷. During the first months of the pandemic, the majority of the tests were serological, but antigen testing has gained high interest recently as this tool can be used for the detection of ongoing viral infection and utilized as a control measure in communities³. Many tests involve detection of the highly abundant coronavirus nucleocapsid (N) and spike (S) proteins, which are considered ideal targets in antigen testing². For example, Hristov *et al.*⁵ showed detection of coronavirus S proteins on a paper-based, sandwich-type LFA immunoassay. Grant *et al.*³ developed a half-strip LFA for the detection of SARS-CoV-2 N proteins. Moreover, Mertens *et al.*⁸ have developed an immunochromatographic assay for the rapid detection of SARS-CoV-2 nucleocapsid from nasopharyngeal specimens.

Additionally, commercial coronavirus home test kits for antigen detection are available from pharmacies or supermarkets⁹⁻¹³. With these tests, the possible infected sample is collected and analyzed on-site, with no need for assistance from healthcare professionals. Thus, such tests can

alleviate the demand for medical facilities and facilitate fast testing for border control and for tracing in schools and workplaces. POC-based tests enable also testing with non-invasive specimens, *e.g.*, saliva or nasal swab, which facilitates convenient sampling¹⁴⁻¹⁶. Unfortunately, the performance of typical rapid tests vary considerably. The current technologies are lacking repeatable results and antigen tests are not considered as reliable as those from RT-PCR¹⁷. Especially, the main challenge for POC tests is the detection of small amounts of proteins. Consequently, there is a critical need for highly sensitive tests. Although specific antibodies against coronavirus antigens are available, the immobilization capacity of the former on sensor substrates is lacking^{18,19}, which results in low bioactivity. Specifically, upon immobilization, the antibodies can lose part of their flexibility, which affects antigen binding and reduces sensitivity. Alternatively, inappropriately attached sensing elements can be washed away with advancing sample fluid. All in all, there is a critical need for new generation substrates for improved antibody immobilization and to ensure efficient, ultra-sensitive antigen detection.

Efforts to improve immobilization should consider the effects of physical adsorption, chemical bonding, or affinity interactions based on biomolecules²⁰. In this context, our recently introduced charged cellulose II nanoparticles, comprising a soft shell and a hard core structure, offer the potential for controlling surface protein interactions. Specifically, we reported cationic cellulose II nanoparticles to effectively increase protein adsorption and antibody immobilization²¹. The cellulose nanospheres interpenetrate and self-assemble into densely packed, viscoelastic, and water-swollen colloidal nanogel layers that are highly accessible to molecules and facilitate specific protein interactions.²¹ Furthermore, anionic, soft shell/hard core cellulose II nanoparticles offer the possibility to further control protein interactions²²⁻²⁴. Earlier reports showed that the corona of the anionic nanospheres can deform and interpenetrate into a colloidal nanogel

structure²². The swelling behavior of such anionic material offer promise to passivate immunoassay supports from non-specific protein adsorption given its hydrophilicity and involved electrostatic interactions.

Supports that facilitate sensitive and rapid detection also need consideration. Commonly, LFAs constructs make use of pads, cellulosic materials, glass fibers, or sintered polymers^{25,26}. They are often glued together *via* a lamination process that enables analyte transport from one area to another²⁵. However, gluing can be impractical in some applications, and the adhesives can block the channel pores, preventing adequate flow. Paper-based fluidic systems may also lack pattern resolution and the complexity of the channel design can be limited^{27,28}. As an alternative for paper-based substrates, we have developed printable wicking materials comprising calcium carbonate particles and micro- and nanocellulose binders that are stencil-printed on flexible paper or polymer substrates, forming fluidic channels²⁹. These printable pastes allow tunable and complex flow channel designs. Besides, the possibility to tailor the paste composition enables modification of wicking properties, useful in regulating fluid flow for specific analyte detection.

In this work, cellulose II nanoparticles are used to control protein interactions on surfaces and to enable highly sensitive and fast SARS-CoV-2 nucleocapsid detection. The involved interactions are investigated by using electromechanical sensing and confocal microscopy. Besides, we demonstrate the use of cellulose nanospheres in printable, flexible immunoassay systems. Cationic nanoparticles are used as an effective anchoring layer, *i.e.*, to immobilize the sensing elements on the given support; meanwhile, negative cellulose particles act as blocking or passivating component, preventing non-specific protein adsorption. The assay system is prepared by stencil printing the fluid-wicking channel on flexible paper support. Moreover, inkjet-printing of the

anchor layer pattern on the channel is carried out and followed by immobilization of the sensing antibodies, enabling the detection of SARS-CoV-2 nucleocapsid (see **Figure 1**).

EXPERIMENTAL SECTION

Materials. Cellulose nanofibrils (CNF) (2.4 wt%) were prepared from bleached Kraft birch pulp fibers by using a microfluidizer (M110P fluidizer, Microfluidics Corp.) equipped with 200- μm and 100- μm chambers operated at 2000 bar using six passes. High-consistency enzymatic fibrillated cellulose (HefCel) (19-23 wt%) and nanopaper (CNF films) were provided by VTT Technical Research Centre of Finland^{30,31}. Microcrystalline cellulose (Avicel), dimethyl sulfoxide (DMSO) ($\geq 99.9\%$), and calcium carbonate (CaCO_3) precipitated for analysis (EMSURE® Reag. Ph. Eur.) was purchased from Merck. PowerCoat® HD, which is suitable for various printing operations such as inkjet, flexo, and screen printing, was provided by Guarro Casas³². SARS-CoV-2 nucleocapsid capture antibody (humanized monoclonal antibody, MAT-8523), SARS-CoV-2 recombinant nucleoprotein positive control (cytoplasmic extract), SARS-CoV-2 nucleocapsid detection antibody (mouse monoclonal antibody, MAT-8524), and SARS-CoV-2 nucleocapsid antibody conjugated with gold nanoparticles (antibody MAT-8524 labeled with AuNP) were kindly provided by Coris BioConcept. Also, SARS-COV-2 Nucleocapsid (aa1-419) His Tag Recombinant protein was purchased from ThermoFisher Scientific. All other chemicals were purchased from Sigma-Aldrich: Fluorescein 5(6)-isothiocyanate (FITC) ($\geq 90\%$), polyethyleneimine (PEI) 50 % aqueous solution (Mw 600 000–1 000 000 g/mol), glycidyltrimethylammonium chloride (dry substance $\geq 90\%$), 2-propanol (2-PrOH), sodium chloroacetate ($\geq 98\%$), urea (BioReagent, $\geq 98\%$), human immunoglobulin G (hIgG) ($\geq 95\%$), anti-human immunoglobulin G (anti-hIgG) γ -chain specific antibody produced in rabbit, anti-

mouse IgG (Fab specific) antibody produced in goat, fibrinogen from human plasma (50-70 % protein), casein hydrolysate, propylene glycol, and bovine serum albumin (BSA) (≥ 98 %). Water purified with a Millipore Synergy UV unit (MilliQ) was used throughout the experiments.

Synthesis of charged cellulose II nanoparticles. Anionic and cationic cellulose nanoparticles were produced following our previous reports^{21,22,33}. First, cellulose II gel was prepared from microcrystalline cellulose (MCC). To transform the native cellulose I into the cellulose II crystal structure, MCC was treated in a NaOH/urea solution. Specifically, 7 wt% NaOH and 12 wt% urea were mixed and stirred. Then, MCC was added into this solution and mixed until a homogeneous slurry was obtained at 5 wt%. The slurry was frozen and stored at -20°C overnight. Next, the slurry was thawed at room temperature and diluted to 1 wt% with DI water, and equilibrated for 1 h. Finally, the sample was washed by dialysis (Spectrum™ Spectra/Por™ 6 Pre-wetted standard RC dialysis tubing, MWCO 1-50 kD). The obtained hydrogel was used for the preparation of anionic and cationic cellulose II nanoparticles.

Cationic cellulose II nanoparticles (NPcat): The prepared cellulose II gel was concentrated by centrifugation at 10 000 rcf for 10 min, to a solids content of ca. 9 wt%. The material (32 g) was transferred into a 100 mL Schott bottle. The suspension was mixed with a 50 wt% aqueous solution of NaOH (0.38 g, 4.8 mmol). After 30 min, glycidyltrimethylammonium chloride (5.5 mL, 6.2 g) was added and the highly viscous gel was mixed with a glass rod and transferred into a water bath at 55°C . After 20 h, the suspension was washed with MilliQ water following three washing and centrifugation cycles (5 min at 10 000 rcf). The suspension was further purified by dialysis against deionized water for 4 days. Finally, the suspension was homogenized in a microfluidizer (2 passes at 2000 bar, Microfluidics M110P, Microfluidics Corp.) to yield individualized spherical nanoparticles.

Anionic cellulose II nanoparticles (NPan): The cellulose II gel was solvent-exchanged to 2-PrOH prior to carboxymethylation. First, 100 mL of the gel (4.0 wt%) was concentrated by centrifugation at 10 000 rcf for 10 min. Then, the concentrated slurry was diluted with 100 mL of technical 2-PrOH, filtrated, and washed with technical 2-PrOH (3 x 100 mL). The solid content of the alcoholic suspension was adjusted to 4 wt%. Next, 1.3 M NaOH solution was added, and after equilibration for 30 min, 2.9 g of sodium chloroacetate was added. The reaction mixture was stirred at 55°C for 4.5 h. The yellowish product was filtered and transferred into a centrifugation tube. Then, the suspension was washed intensively with deionized water by a set of washing and centrifugation (5 min at 4000 rcf) steps until gaining neutral pH. Finally, the centrifugation time was increased to 30 min. After washing, the opaque aqueous suspension was diluted to a solids content of 1.4 wt% and homogenized in a high-pressure homogenizer at 800 bar using 4 cycles, yielding a translucent suspension. Following, this suspension was centrifugated for 5 min at 4000 rcf to remove small amounts of residual, coarse particles.

Nanoparticle characterization. *Zeta-potential and particle size:* Zetasizer (Zeta sizer Nano ZS 90, Malvern) was used to measure the zeta-potential and particle size using 0.05 wt% NPan and NPcat suspensions in 2.5 mM NaCl. Six replicates were measured with each sample. *Atomic force microscopy (AFM):* AFM (MultiMode 8 Scanning Probe Microscope, Bruker AXS Inc.) was used to analyze the surface topography of the NPcat and NPan particles deposited on SiO₂ wafers. Surface areas of 5 x 5 μm², 3 x 3 μm² and 1 x 1 μm² were investigated in air by using AFM tapping mode with silicon cantilevers (NSC15/AIBS, MicroMasch). Three different areas on each sample were imaged and flattening was used for image processing. *Fourier-transform infrared spectroscopy (FTIR):* To show successful modifications, infrared spectra of the freeze-dried nanoparticles was measured with the FTIR (Spectrum Two FT-IR Spectrometer, PerkinElmer).

Stencil printing of fluidic channels on paper. To prepare porous substrates for immunoassays, fluidic channels were stencil printed on PowerCoat[®] paper supports according to our previously reported method²⁹. Briefly, a stencil-printable paste was prepared by mixing CaCO₃, CNF, and HefCel. First, CaCO₃ was dispersed in DI water. Then, CNF and HefCel were mixed with the CaCO₃ paste until a homogeneous dispersion was obtained. The prepared paste is hereafter referred to as Ca-CH, denoting a composition that included CaCO₃, CNF, and HefCel at a dry weight ratio of 95:2.5:2.5. This paste had 10 g of total solids in the dry state, whereas the solids content of the wet paste was 37.0 wt%. Besides, to improve adhesion to the hydrophobic PowerCoat[®] paper, propylene glycol (5 wt% of the wet paste) was added to the paste formulation. Finally, fluidic channels were printed on a PowerCoat[®] paper using a stencil with desired pattern dimensions. A squeegee (RKS HT3 Soft) was used to transfer the paste on paper through a plastic stencil (350 μm thickness) following a circular pattern ($r = 5$ mm) used as a sample deposition area. A rectangular section (4 x 70 mm²) was used for fluid flow transfer to the detection zone. Stencil printing of fluidic channels is illustrated in **Figure S1**.

Preparation of model films for quartz crystal microgravimetry. To study protein interactions on the printed fluidic channels, thin model films were prepared from the diluted Ca-CH paste, and the adsorption behavior of various proteins on these films was studied by quartz crystal microgravimetry with dissipation monitoring (QCM-D). Before the film preparation, CaCO₃ was ball-milled for 40 min to decrease the particle size and filtered. The Ca-CH paste was prepared as described above and diluted with MilliQ water to a solids content of 22.8 wt%. Then, the diluted sample was drop-cast onto UV-ozonized QCM-D crystals (QSX 301 Au, Biolin Scientific) with a thin anchor layer of polyethyleneimine (PEI) and washed with MilliQ to remove any loosely bound material.

Scanning Electron Microscopy (SEM). The printed fluidic channels and the corresponding thin model films deposited on QCM-D crystals were imaged using an SEM. Before imaging, all the samples were sputter-coated with a 4-nm Au-Pd layer using a LEICA EM ACE600 sputter coater. Images of the channels were taken with a field emission microscope (Zeiss Sigma VP) operated at 1.5 kV.

Quartz crystal microbalance with dissipation monitoring (QCM-D). QCM-D (E4 instrument, Q-Sense AB) was employed to monitor protein adsorption on the model surfaces at pH 7.4. Changes in the sensor oscillation frequency were measured at a fundamental resonance frequency of 5 MHz. All measurements were performed at 23 °C, under a constant flow of 100 $\mu\text{L}/\text{min}$. Each sample was measured at least twice. The adsorbed mass was calculated following the Sauerbrey equation (Equation 1):

$$\Delta m = -C_{QCM} \frac{\Delta f}{n}, \quad (1)$$

where C_{QCM} is 17.7 ng/(Hz \times cm²) for 5 MHz crystal, Δf is the change in frequency, and n is the overtone number^{34,35}. In addition, Voigt viscoelastic modeling (Q-Tools software, version 2.1 Q-Sense) was used to estimate the effect of viscoelastic property changes of the film on the adsorbed protein mass. In the model, the fluid density and viscosity were set to 1000 kg m⁻³ and 0.001 m³ kg⁻¹, and the density was approximated to be 1300 kg m⁻³ for the adsorbed protein layer³⁶.

Prior to measurement, the model films were placed inside QCM chambers and stabilized in a phosphate buffer (pH 7.4, 10 mM) until a stable baseline was obtained. First, non-specific protein interactions and the effect of NPcat and NPan on adsorption were studied and their performance was compared with typical anchoring and blocking materials. The adsorption of 0.01 mg/mL BSA was first monitored on unmodified, PEI-, NPcat- and NPan-treated model surfaces. The cationic materials were used as anchor layers to improve the extent of adsorption on the surfaces, whereas

anionic nanoparticles were used as blocking material. The PEI, as a cationic polymer, is commonly used as coating material, adhesive, surface modifier, and anchoring layer for different polymers and cell cultures³⁷⁻⁴⁰. The material treatments were done by injecting 0.5 wt% aqueous solutions of each material onto the model films *in situ* in the QCM unit before adsorption of the proteins. Similarly, adsorption of 0.01 mg/mL fibrinogen was monitored on unmodified, PEI-, NPcat-, bovine serum albumin (BSA)- and NPan-treated model surfaces. BSA is typically used as a blocking agent. The BSA blocking effect was compared to that of NPan. Finally, non-specific adsorption of SARS-CoV-2 nucleocapsid (6 ng/mL) was measured on BSA-blocked model surfaces. Notably, phosphate buffer was used for washing after each adsorption step.

In addition, specific interactions and detection of SARS-CoV-2 nucleocapsid (N protein) were investigated with QCM-D experiments using unmodified, PEI- and NPcat-treated model surfaces. The cationic materials were used as immobilization agents for the capture antibodies. Specifically, after stabilization in phosphate buffer, the capture antibodies (20 µg/mL SARS-CoV-2 nucleocapsid antibody in buffer) were adsorbed on the model surfaces. Then, washing was carried out with the buffer solution to remove unbound antibodies. 10 µg/mL BSA solution was used to block the remaining non-specific binding sites. Next, N protein (6 ng/mL) was introduced, following by a buffer washing step. Finally, the adsorption of detecting antibodies (20 µg/mL) was monitored and loosely bound particles were removed by washing with the buffer. These kinds of interactions occur typically in the test line of a sandwich-type immunoassay. We also studied the adsorption behavior of human immunoglobulin G (hIgG) to its secondary antibody, anti-hIgG, to represent the interactions that typically occur on the control line of immunoassays. First, 20 µg/mL anti-hIgG was adsorbed on the model surfaces. Then, 10 µg/mL BSA blocking agent was applied followed by adsorption of 10 µg/mL hIgG. Notably, washing with buffer was done between each

adsorption step. The interactions between hIgG and anti-hIgG were studied on the PEI- and NPcat-treated model films.

Fluorescein labeling of hIgG. Antibodies were modified with a fluorescent probe by using the procedure of Hermanson⁴¹ with few alterations. First, 2 mg/mL protein solution was prepared in 0.1 M sodium carbonate buffer (pH 9.0). Then, 1 g/L FITC solution was prepared in a dark room by dissolving FITC in dry DMSO. This solution was protected from light by wrapping the bottle using aluminum foil. Next, 100 μ L of the FITC solution was added dropwise to each mL of hIgG solution and gently mixed. The reaction occurred at 4 °C for 8 h. To purify the obtained FITC-stained hIgG (hIgG-FITC) from unreacted FITC molecules, the solution was centrifuged four times at 4000 rpm for 30 min by using centrifugal filter units (Amicon Ultra-15, MWCO 30 kDa).

Protein adsorption and confocal laser scanning microscopy (CLSM). To further demonstrate the immobilization capability of NPcat and the blocking effect of NPan, the non-specific adsorption behavior of hIgG-FITC was studied on filter paper and printed fluidic channels supported on PowerCoat[®] HD. First, 3 μ L of 0.5 wt% PEI, NPcat, or NPan were adsorbed on the substrates. The substrates were, then washed with MilliQ; filter papers were fully immersed in water and the printed fluidic channels were washed by pipetting water on the channel. Next, 10 μ L of 0.1 mg/mL hIgG-FITC (in phosphate buffer, pH 7.4) was adsorbed on the samples, followed by buffer washing. Finally, the hIgG-FITC exposed samples were imaged with CLSM to detect the adsorbed antibodies. Images were taken with a laser scanning spectral confocal microscope (Leica TCS SP2, Leica microsystems CMS GmbH) by using 488 nm excitation wavelength and 500-540 nm detection wavelength range. Images were acquired using a 750 V laser power and under constant imaging conditions. The intensity of fluorescence of each confocal image was determined using Adobe Photoshop 2021.

Inkjet-printing of patterns with cationic materials. An inkjet printer (Dimatix Materials Printer, DMP-2831, Fujifilm) was used to print NPcat and PEI patterns on top of filter papers, nanopapers, and printed Ca-CH channels. First, 0.5 wt% NPcat solution was filled in DMC-11610 cartridges (10 pl nominal drop volume) and printed using a drop spacing of 20-40 μm at 2 kHz frequency, 35 V jetting voltage, and 3-inch H_2O meniscus vacuum. Alternatively, 0.5 wt% PEI solution was printed on the substrates with a drop spacing of 20-40 μm at 3 kHz frequency, 24 V jetting voltage, and 3-inch H_2O meniscus vacuum. Various designs and pattern sizes were tested and 1-10 layers of material were printed, depending on the substrate thickness and material type. In addition, cleaning was done with the “Purge 0.1s” cleaning cycle at the beginning and end of the printing. *Dye adsorption test.* The adsorption capabilities of printed NPcat and PEI patterns were studied with a fluorescein-based dye. First, 0.05 wt% dye solution was dropped on the patterned substrates with a pipette. Then, the substrates were washed with MilliQ water; the filter paper samples were fully immersed in water, whereas the printed fluidic channels were washed by pipetting water onto the channel. The formation of the patterns was evaluated by visual observation. *Protein interactions and confocal imaging.* We studied protein adsorption onto NPcat- and PEI-patterns printed on nanopapers. These films were prepared from cellulose nanofibrils (CNF) and were thin enough to permit the detection of the patterns with confocal microscopy. Specifically, 10 μL of 0.1 mg/mL hIgG-FITC (in phosphate buffer, pH 7.4) was adsorbed on the films with NPcat and PEI print patterns. Then, washing was done with the buffer. Next, the samples were imaged with CLSM by using 633 V laser power and constant imaging conditions. Additionally, specific protein interactions were studied using similar methods. First, 10 μL of 0.1 mg/mL anti-hIgG was adsorbed on the printed patterns and washed. Then, 10 μL of 0.5 wt% BSA was added and washed. Finally, 10 μL of 0.1 mg/mL hIgG-FITC was introduced,

and after washing, the samples were imaged with CLSM. The specific interactions between hIgG and anti-hIgG were also investigated using nanopaper, in the absence of any anchor layers.

Coronavirus antigen detection with patterned sensors. *Preparation of the assay:* Fluidic channels were treated with NPan to block the non-specific binding sites. An inkjet printer (Dimatix Materials Printer, DMP-2831, Fujifilm) was used to form NPcat patterns on the testing and control areas of the fluidic channels. The NPcat was printed with a drop spacing of 40 μm at 2 kHz frequency, 35 V jetting voltage, and a 3-inch H_2O meniscus vacuum. Two NPcat layers were printed on the test area forming a “+” pattern ($2.2 \times 2.2 \text{ mm}^2$) and 3 layers were printed on the control area to form an “OK” pattern ($3.5 \times 2 \text{ mm}^2$), **Figure S2**. To deposit the sensing elements, 3 μl of capture antibody solution (0.1 mg/mL) was drop-cast on top of the “+” NPcat pattern. The control pattern (“OK”) was tested with and without antibodies. Thus, the pattern was either left untouched or 3 μl of secondary antibody solution (0.5 mg/mL) was dropped on top of the printed pattern. Then, washing was carried out with phosphate buffer (pH 7.4, 10 mM) to remove loosely bound molecules. Next, BSA (0.5 wt%) was used to block the remaining uncovered NPcat areas on the test zone, and also on the control zone, if antibodies were applied. Finally, washing was done with the buffer and the assays elements were dried before testing. *Coronavirus antigen sensing:* Detection of the SARS-CoV-2 nucleocapsid was performed with the dried assays. Analysis was first done by testing antigen-positive (with N protein) and -negative (without N protein) samples in buffer solution. The negative sample contained 2 wt% casein hydrolysate, 1 wt% fibrinogen, and AuNP-labeled detection antibodies (with an optical density of 0.5). Casein and fibrinogen were used as non-specific proteins. The positive sample contained 0.4-1000 ng/mL N protein, 2 wt% casein hydrolysate, 1 wt% fibrinogen, and the detection antibodies (OD 0.5). Also, antigen-positive and -negative saliva samples were tested. The negative sample was prepared

by mixing saliva and buffer solution with AuNP-labeled detection antibodies, 1:1 ratio. The positive sample was prepared by mixing saliva with added N protein (final concentration 1 $\mu\text{g/mL}$) and buffer solution with AuNP-labeled detection antibodies in a 1:1 ratio. All samples were analyzed by drop-casting 40 μL of solutions on the circular sample area of the prepared assays. Analysis of the results was done after 2–15 min. A positive result was indicated with color development in both, the control and test areas. A negative result was indicated with color development in the control area. An invalid test/positive result was analyzed if only the test area developed color.

RESULTS AND DISCUSSION

Cellulose II nanoparticles. Following previous publications^{21–23,33}, the introduction of repulsive charges to amorphous regions of cellulose II hydrogels and the combination of mechanical treatment produced charged soft cellulose II nanospheres. Anionic cellulose II nanoparticles (NPan) were obtained by carboxymethylation, whereas cationic cellulose II nanoparticles (NPcat) were produced following reaction with glycidyltrimethylammonium chloride. The FTIR spectra of these materials (**Figure S3**) indicated a carbonyl band (approx. 1610 cm^{-1}) in the spectrum of NPan and a C-N band (approx. 1510 cm^{-1}) in the spectrum of NPcat, corresponding to the introduction of cationic trimethylammonium moiety and confirming the successful carboxymethylation and cationization. Additionally, the colloidal properties of the nanoparticles are summarized in **Table S1**. The unique feature of the hard core/soft shell cellulose nanospheres involves self-assembly into densely packed colloidal nanogel layers, which are applied to control protein interactions on cellulose thin films and paper^{21,22}. Furthermore, the AFM images showed surfaces fully covered with the nanospheres, **Figure S4**.

Printed fluidic channels. The fluidic channels printed on PowerCoat[®] paper, **Figure S5**, showed repeatable designs obtained by stencil printing. The fluid wicking properties of these channels have been analyzed in our previous work, where we reported that the channels wicked 4 cm of water in approx. 130 s²⁹. In addition, SEM images of the channel surfaces showed a porous network formed by the cubic-shaped inorganic filler and cellulose micro- and nanofibrils, used as binders, **Figure S6**.

Protein interactions. QCM-D was used to monitor protein adsorption and interactions between the coronavirus antigen and the sensing elements, which would later be employed in antigen-sensing immunoassay. The measurement was first done on thin films used as models of the printed fluidic channels. The model films were prepared by casting diluted CaCO₃-CNF-HefCel (Ca-CH) paste on QCM crystals. The SEM images of the cast films are presented in **Figure S7**. Noteworthy, the prepared model films were not as porous as the macroscale fluidic channels, considering that the effect on adsorption of the three-dimensional structure of the paste could not be observed with this method. Besides, the effect of specific cationic treatment of the model films on protein adsorption was studied. These treatments were carried out with NPcat or PEI, which enabled model films with higher adsorption capability. The AFM images of unmodified, NPcat- and PEI-treated surfaces are included in **Figure S8**.

Non-specific binding of BSA was studied with unmodified, PEI-, NPcat- and NPan-treated model surfaces and to demonstrate the ability of the nanoparticles to control protein interactions. The frequency changes of the oscillating QCM sensors, after BSA injection, can be seen in **Figure 1c**. The calculated adsorbed protein mass is included in **Table 1** and the measured shift in energy dissipation during adsorption is listed in **Table S2**. The adsorbed protein mass was estimated with the Voigt model, namely, to correlate the viscoelastic changes with the protein mass. For

comparison, the values of adsorbed mass obtained with the Sauerbrey approximation were also calculated. NPcat increased significantly BSA adsorption, by 111 %, whereas NPan reduced interactions by 98 %. Hence, 637 ng/cm² adsorbed BSA mass was obtained for the unmodified surface, while 1345 ng/cm² and 14 ng/cm² were obtained for the NPcat and NPan, respectively. Furthermore, BSA adsorption on the PEI-treated surface corresponded to 515 ng/cm², which was 19 % lower than on the unmodified surface.

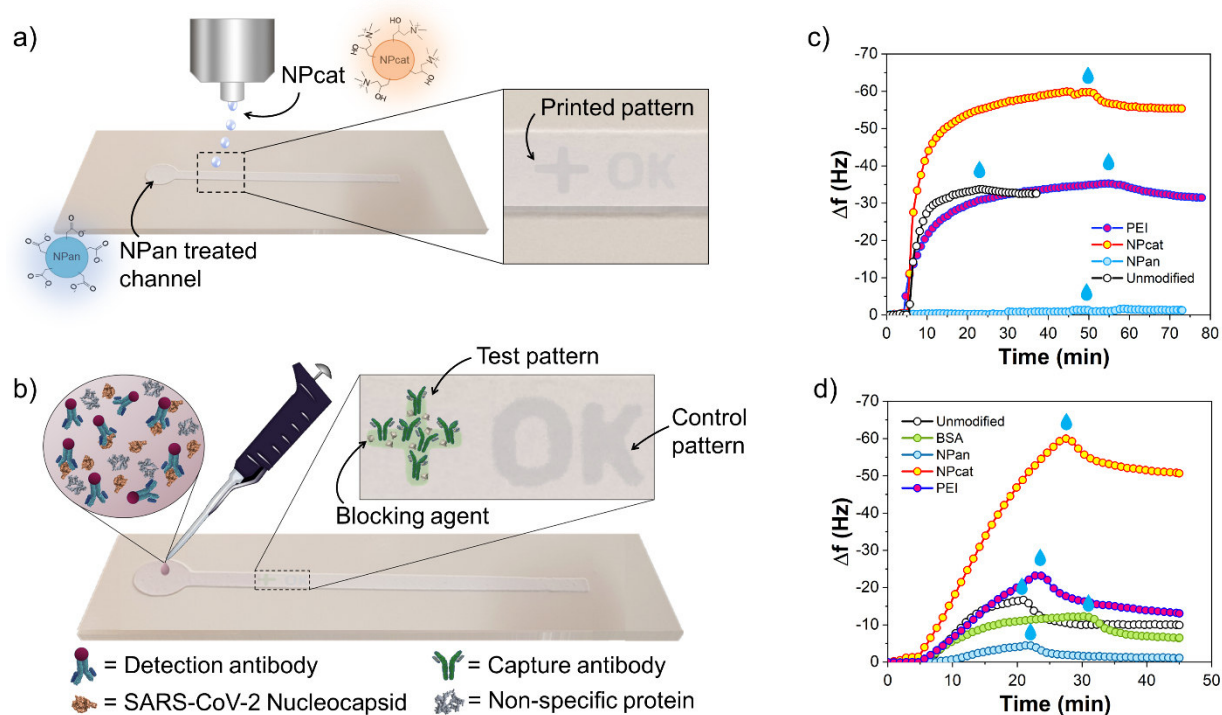


Figure 1. Use of cellulose II nanoparticles in a colorimetric immunoassay for detection of SARS-CoV-2 nucleocapsid on stencil printed fluidic channels: a) Anionic cellulose II nanoparticles (NPan) are used to passivate the assay substrate from non-specific protein adsorption. Cationic cellulose II nanoparticles (NPcat) are inkjet-printed, forming anchoring patterns, to later form the assay sensing areas. b) Nucleocapsid-specific capture antibodies are immobilized on the test pattern while the control pattern is left unmodified. The test pattern is carefully blocked with BSA

to ensure specific detection. Testing is performed with samples containing labeled detection antibodies, non-specific proteins, and antigens. QCM-D sensograms demonstrating the ability of cellulose II nanospheres to control surface protein adsorption: c) BSA adsorption on unmodified, PEI-, NPcat- and NPan-treated model surfaces. d) Fibrinogen adsorption on unmodified, PEI-, NPcat- and NPan-treated model surfaces, blocking efficiency of NPan also compared to BSA-blocked model surfaces (unmodified treated with BSA).

Table 1. Calculated BSA and fibrinogen adsorbed mass on the given model surface.

BSA		
Surface	Voigt (ng/cm²)	Sauerbrey (ng/cm²)
Unmodified	637	576
PEI	515	571
NPcat	1345	981
NPan	14	23.8
Fibrinogen		
Surface	Voigt (ng/cm²)	Sauerbrey (ng/cm²)
Unmodified	188	176
PEI	205	232
NPcat	858	896
NPan	18	19.9
BSA	137	113

Protein interactions were studied with another non-specific protein, fibrinogen, which is a complex, fibrous glycoprotein, larger than the globular BSA. Fibrinogen adsorption isotherms on the unmodified, BSA-, NPan-, PEI-, NPcat-treated surfaces are included in **Figure 1d**, and the calculated adsorbed masses are listed in **Table 1**. The measured dissipation changes are shown in

Table S2. The adsorption of fibrinogen on the unmodified surface was 188 ng/cm², while PEI- and NPcat-treated surfaces adsorbed 205 and 858 ng/cm², respectively. Thus, NPcat-modification increased adsorption by 356 %, whereas only a small increase (9 %) was obtained following PEI treatment. The blocking efficiency of NPan was compared with BSA, a commonly used blocking agent. NPan blocked fibrinogen adsorption more effectively, by 90 % (18 ng/cm²), compared to the unmodified surface or the BSA-blocked surface (reduced adsorption by 27 %, 137 ng/cm²). Therefore, NPan was used as a blocking agent for the immunoassay substrates. BSA was also used to ensure the specificity of the sensor by blocking exposed NPcat sites between capture antibodies in the assay sensing area.

The QCM-D technique was also employed to monitor coronavirus antigen detection. The studied interactions between antibodies and N protein were later utilized in the development of the coronavirus antigen test since they occur on the test area of the assay. **Figure 2a-c** shows the measured frequency and dissipation changes upon antibody and antigen interactions with the unmodified, NPcat- and PEI-treated surfaces. First, capture antibodies (humanized monoclonal SARS-CoV-2 nucleocapsid antibody) (1) were adsorbed on each surface. Then, BSA (2) was used to block the remaining non-specific binding sites, and finally, specific adsorption of the antigen (SARS-CoV-2 N protein) (3) and the detection antibody (mouse monoclonal SARS-CoV-2 nucleocapsid antibody) (4) were measured. To show the difference in binding of each surface, the cut QCM-D data of antibody and antigen adsorptions are presented in **Figures 2d-f**. Both cationic materials increased the binding of the capture antibody. The Voigt viscoelastic modeling was employed to calculate the adsorbed mass since the measured dissipation changes on each surface (**Figure 2a-c**) indicated that the adsorbed layers were soft and viscoelastic. The results were also compared to the Sauerbrey values (**Table 2**). Compared to the calculated adsorbed mass on the

unmodified surface (474 ng/cm^2), we measured a 64 % higher adsorption of the capture antibody on PEI-treated surface (777 ng/cm^2) and 83 % higher on the NPcat-treated surface (867 ng/cm^2). The detection of antigen was analyzed on each surface upon BSA treatment. The antigen mass obtained for unmodified, PEI- and NPcat-treated surfaces, corresponding to 115, 28, and 194 ng/cm^2 , respectively. Thus, the highest adsorption of N protein was obtained with NPcat-treated supports (**Figure 2e**). Most likely, improved immobilization of the capture antibody led to higher antigen binding. On the other hand, the PEI-treated surface showed limited adsorption of the antigen, despite the increased antibody binding effect following PEI treatment. It is possible that the PEI surface adsorbed the capture antibodies in a non-active conformation, reducing the binding of the antigen. In addition, **Figure 2e** shows only minor non-specific adsorption of the antigen on the BSA-blocked model surface, revealing that the capture antibody is required to bind the antigen onto the surface. Furthermore, the NPcat surface facilitated better adsorption of the detection antibody (88 ng/cm^2) compared to the unmodified surface (27 ng/cm^2) (**Figure 2f**). The residual amount after washing of detection antibody on the NPcat-treated surface was higher compared to the unmodified sample as well as the PEI-treated surface. In fact, the latter did not adsorb significant amounts of the detection antibody.

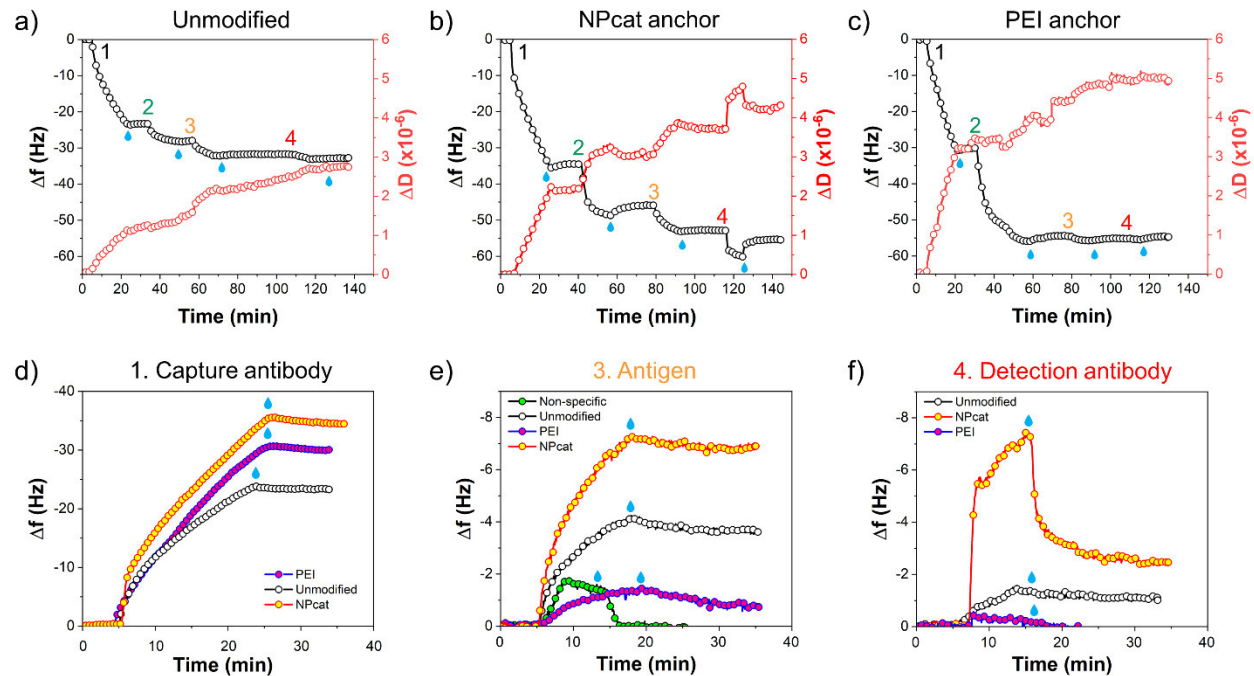


Figure 2. QCM-D sensograms (frequency and dissipation shift) upon adsorption of (1) capture antibody, (2) BSA, (3) SARS-CoV-2 nucleocapsid, and (4) detection antibody on a) unmodified, b) NPcat-treated and c) PEI-treated model surfaces. Effect of surface treatments on the detection can be seen by comparing the adsorption steps: d) adsorption of capture antibody on unmodified, PEI-, and NPcat-modified surface, e) adsorption of antigen (N protein) after BSA-blocking on each surface, adsorption curve for non-specific antigen binding to BSA-blocked model surface is given as comparison, f) adsorption of detection antibody on each surface.

Table 2. Adsorbed masses of the coronavirus antibodies and antigen on each surface.

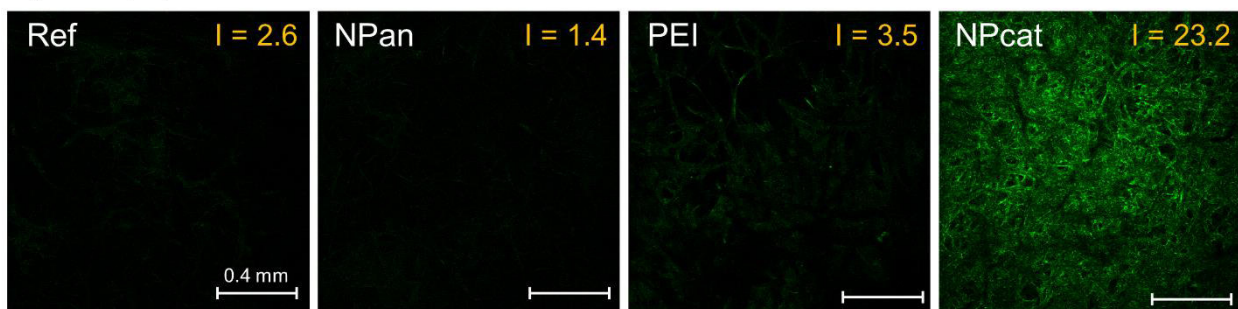
Surface	Adsorbed protein	Δm_{Voigt} (ng/cm ²)	$\Delta m_{\text{Sauerbrey}}$ (ng/cm ²)
Unmodified	Capture antibody	474	412
	N protein	115	63
	Detection antibody	27	18
NPcat-treated	Capture antibody	867	609
	N protein	194	119
	Detection antibody	88	45
PEI-treated	Capture antibody	777	529
	N protein	28	14
	Detection antibody	-	-

We studied the effect of cationic treatments on hIgG interactions with its secondary antibody, anti-hIgG. These kinds of interactions typically occur on the control line of an immunoassay. The adsorption results can be seen in **Figure S9**. Similarly, increased immobilization capability was obtained with the NPcat treatment compared to the unmodified and PEI-treated surfaces.

Protein adsorption and confocal microscopy. To translate the QCM-D results to paper-based systems, the effect of surface treatment on antibody adsorption was studied by confocal microscopy employing filter papers and printed fluidic channels. The non-specific adsorption of human IgG with a fluorescent tag (hIgG-FITC) can be seen on unmodified (Ref), NPan-, PEI, and NPcat-treated substrates, **Figure 3**. The test results corresponding to filter paper (**Figure 3a**) showed only minor antibody adsorption on the unmodified surface (intensity of fluorescence $I=2.6$), and even smaller quantities were detected after NPan treatment ($I=1.4$), demonstrating its blocking efficiency. Oppositely, both cationic treatments increased adsorption of hIgG-FITC, while NPcat showed a significantly higher fluorescence intensity ($I=23.2$) compared to PEI ($I=3.5$). The effect of the treatments on protein adsorption followed the same trend on the printed

fluidic channels (**Figure 3b**) with generally higher fluorescence intensity. This difference is most likely related to the washing procedures of the substrates: filter paper could be completely immersed in the washing buffer, whereas the printed channel could only be washed by pipetting buffer onto the printed channel. In **Figure 3b**, the unmodified printed fluidic channel showed clear non-specific adsorption ($I=10.3$), indicating that blocking was needed for this substrate. The NPan-treatment reduced adsorption, and a measured fluorescence value of 3.5 was obtained. The fluorescence values for PEI- and NPcat-treated samples were 24.8 and 50.4, respectively. Thus, the highest adsorption of hIgG-FITC was obtained with the NPcat. We also compared the blocking effect of NPan with BSA (**Figure S10**). BSA had only a minor effect on non-specific adsorption and quite similar intensity of fluorescence as that for the unmodified substrate (on the printed channel $I=9.2$ and the filter paper $I=2.2$).

a) Filter paper



b) Printed fluidic channel

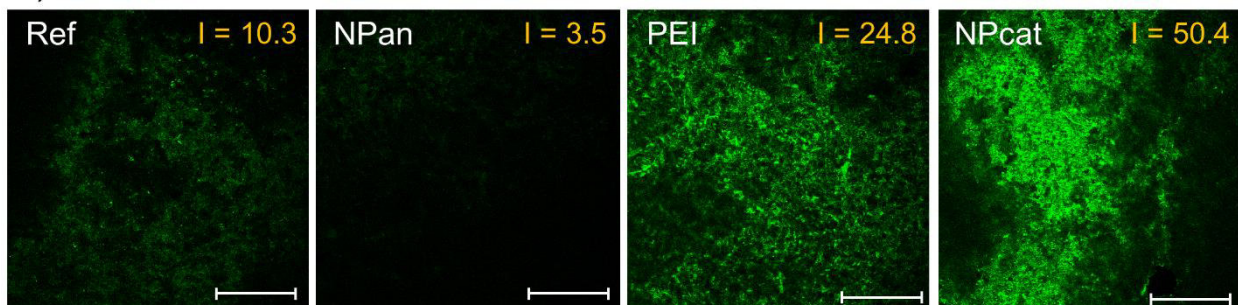


Figure 3. Confocal images of a) filter paper and b) printed fluidic channels exposed to fluorescent-labeled proteins (hIgG-FITC) and the effect of surface treatments on protein adsorption. The fluorescence intensity, I , is indicated in each image. Scale bar in each image 0.4 mm.

Inkjet-printing of cationic patterns. We studied the printing capability of the anchor layers, namely PEI and NPcat, on filter papers, printed fluidic channels, and nanopapers. The successful deposition of the cationic inks was visualized by adsorption of a negatively charged dye on the substrates with the printed patterns (**Figure S11a**). After washing, used to remove the non-adsorbed dye, the printed patterns became visible. The patterns were printed on both filter paper and printed fluidic channels (**Figure S11**). In comparison to NPcat, PEI prints were blurry and had lower resolution. Furthermore, the printing of more than one layer on the substrate was not possible with PEI, whereas multiple NPcat layers were successfully printed, with consistent resolution. These effects for PEI-prints are ascribed to the weaker adhesion of PEI to the substrate.

By using confocal imaging, we determined higher antibody adsorption on printed NPcat and PEI patterns. **Figure 4** shows images of the unmodified, PEI- and NPcat-patterned nanopapers exposed to fluorescent-labeled antibodies. Both non-specific (**Figure 4a, c, e**) and specific (**Figure 4b, d, f**) interactions are shown. Without an anchor pattern, the binding of the antibodies was minor, and only slight fluorescence was detected in both non-specific (**Figure 4a**) and specific (**Figure 4b**) adsorption tests. By contrast, clear fluorescent patterns were detected on the samples treated with PEI- and NPcat anchor prints, indicating that significantly higher amounts of the antibodies were bound to the printed patterns. Interestingly, both patterns showed higher intensity after specific interactions. In addition, the confocal images of the NPcat and PEI patterns, without

the fluorescent-tagged antibodies, can be seen in **Figure S12**. The patterns had only low background fluorescence in the absence of the adsorbed antibodies.

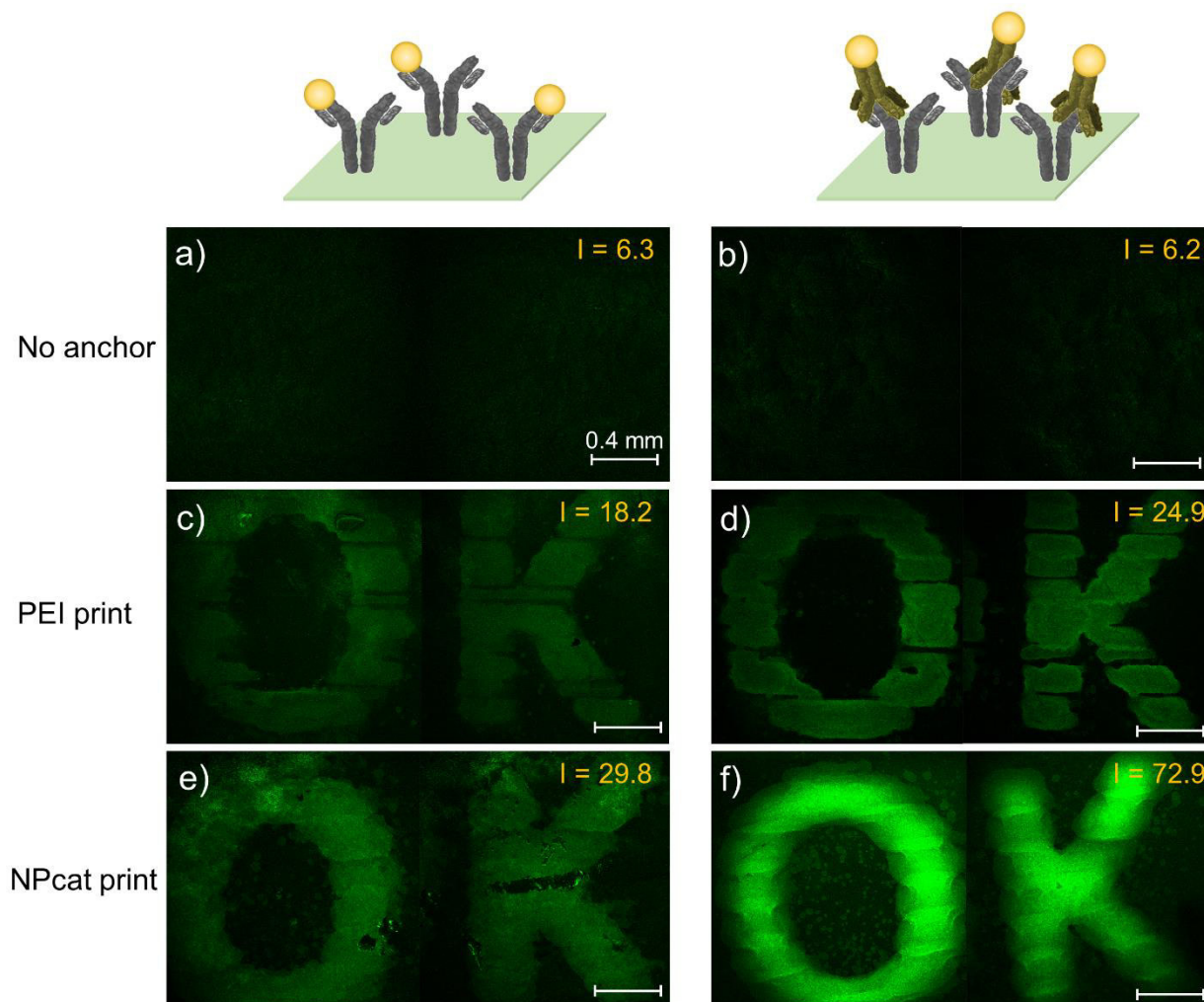


Figure 4. Confocal images showing non-specific (left) and specific (right) protein adsorption onto a-b) unmodified nanopaper, and nanopapers printed with c-d) PEI and e-f) NPcat patterns. In non-specific interactions, hIgG-FITC was adsorbed directly on the samples. For specific interactions, hIgG-FITC was adsorbed on anti-hIgG-treated samples. Imaging was done after washing samples with a buffer solution. The fluorescence intensity is indicated in each image. Scale bar in each image 0.4 mm.

Detection of coronavirus protein. Coronavirus antigen tests were prepared on the printed fluidic channels by employing a sandwiched immunoassay system. Usually, in this type of assay, the analyte is absorbed and transported along a paper strip. The analyte passes first a pad containing antibodies with a detectable label. Here the target antigens bind to the conjugate antibodies and travel further in the channel. When the antigens reach the sensing area, they bind to highly specific test antibodies, which are immobilized on the substrate, and thereby a detectable signal is produced identifying the infection. Generally, a so-called control line is set after the test line to ensure the test worked properly. In the control line, the conjugate antibodies bind to its secondary antibodies, producing the signal with both positive and negative samples. In this work, a similar approach was utilized after few alterations, **Figures 1 and 5**. First, the substrate was passivated from non-specific protein adsorption with NPan. Then, NPcat was used to print anchor patterns on the assay sensing area to immobilize capture antibodies. As shown in **Figure 5a**, the capture antibodies were placed on the test zone on top of the test pattern (“+”), but the control pattern (“OK”) was left untouched. Noteworthy, the test pattern was blocked carefully with BSA to ensure specific detection of the N protein and to prevent false-positive results. The detection of the target analyte was based on induced color reaction upon specific adsorption of the antigen to an AuNP-labeled detection antibody and the immobilized capture antibody (sandwich structure). A visible color emerged when the AuNP-labeled detection antibodies were concentrated on the test pattern. In this test system, the detection antibodies were mixed directly in the sample solution instead of a separate conjugate pad layout (**Figure 5a**). Furthermore, since proteins have a high affinity with NPcat, the detection of the control pattern was enabled by the non-specific binding of the detection antibody to the NPcat pattern. We also tested a sensor system with deposited secondary antibodies on the control pattern. Both positive and negative results could similarly be obtained with this approach.

The test results of this system and illustrations of the possible interactions are included in **Figure S13**.

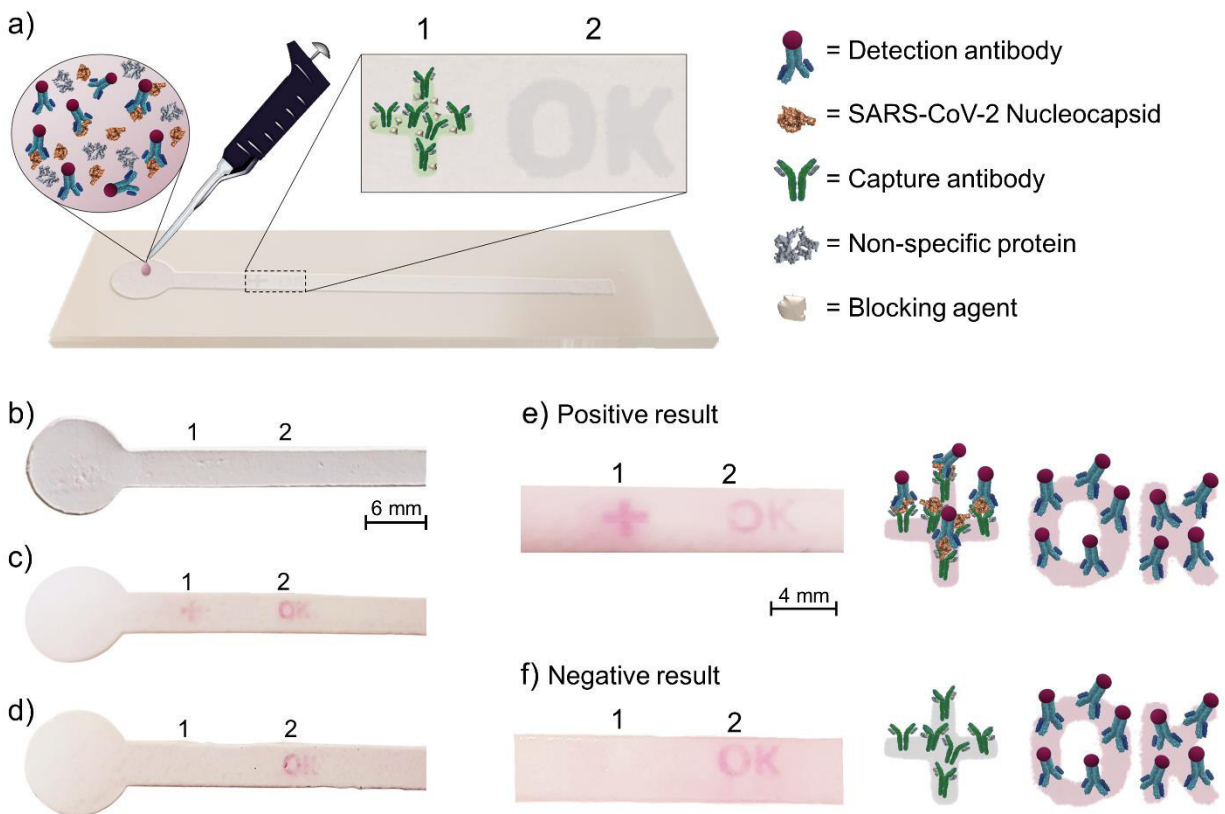


Figure 5. Performance of the introduced, rapid SARS-CoV-2 antigen test: a) Schematic illustration of the prepared assay: Printed NPCat patterns formed the test (“+”) and control (“OK”) patterns of the sensor. The test area (1) was treated with capture antibodies and blocker while the control area (2) was left untouched. The assays were tested with the antigen-positive (coronavirus N proteins, non-specific proteins, and detection antibodies labeled with AuNP-tag in buffer), and antigen-negative (non-specific proteins, and detection antibodies in buffer) samples. Images of cropped immunoassays showing colorimetric responses before and after testing: b) untested assay with marked positions of the test (1) and control (2) areas (patterns invisible), tested and washed

assays exposed to c) antigen-positive sample (8 ng/mL N protein) and d) antigen-negative sample. Schematic illustrations of the protein interactions on the sensing area and corresponding color development in unwashed assays: e) antigen-positive sample and f) antigen-negative sample.

Figures 5b-f show images of the cropped assays and the test results (images with the paper background in **Figure S14**). An untested assay can be seen in **Figure 5b**, where no visible patterns are apparent. However, after testing antigen-positive (**Figure 5c** and **e**) and antigen-negative (**Figure 5d** and **f**) samples, appropriate color developed on the patterns. The positive sample with 8 ng/mL N protein caused a reaction on both the test and control patterns while the negative sample caused color only on the control pattern. The formation of the color was very fast, and a readable result could be obtained within 2 min. Still, to ensure the formation of a negative result, 10-min analysis time was applied. Furthermore, the background adsorption on the test substrate was quite low after washing the samples (**Figures 5c** and **d**). A pale pink color could be seen before washing (**Figures 5e** and **f**) despite the NPan blocking, which is reasoned by the used test layout, which requires a separate washing step to remove loosely bound proteins. In commercial systems based on conjugate pad layouts, the sample itself dilutes and washes the excess detection antibodies during testing. Our system can be regarded, as a proof-of-principle, and the other testing layout could be easily adapted.

The significance of the nanoparticle treatments on sensor performance is highlighted in **Figure 6**, where cropped images of the assays with and without nanoparticle treatments are presented (images with the paper background can be seen in **Figure S15**). If the substrate was not blocked with NPan, significant non-specific adsorption took place even after washing (**Figure 6a**). A high amount of detection antibodies adsorbed especially on the edges of the channels, without the

blocking treatment, and strong color developed from the NPcat patterns when capture antibodies and other proteins were not present (only detection antibodies in the sample). Background adsorption and non-specific binding of the detection antibody on the test pattern was prevented by NPan blocking, and deposition of the capture antibody followed by BSA blocking (**Figure 6b**). Thus, when testing an antigen-negative sample, only control pattern adsorbed detection antibodies (**Figure 6b**), but the observed color was not as strong as seen in **Figure 6a**. The reduced color intensity is due to the competitive, non-specific adsorption of other proteins (casein and fibrinogen), which were present in the sample solution. However, a clear “OK” pattern was observed. The use of NPcat as an anchor layer is required, as shown in **Figure 6c**. No detectable signal could be observed without immobilization of the sensing elements (capture antibody and secondary antibody) with the NPcat. Most likely, many of the antibodies were washed away with the flowing liquid, preventing N protein detection (schematic illustration included in **Figure S13a**).

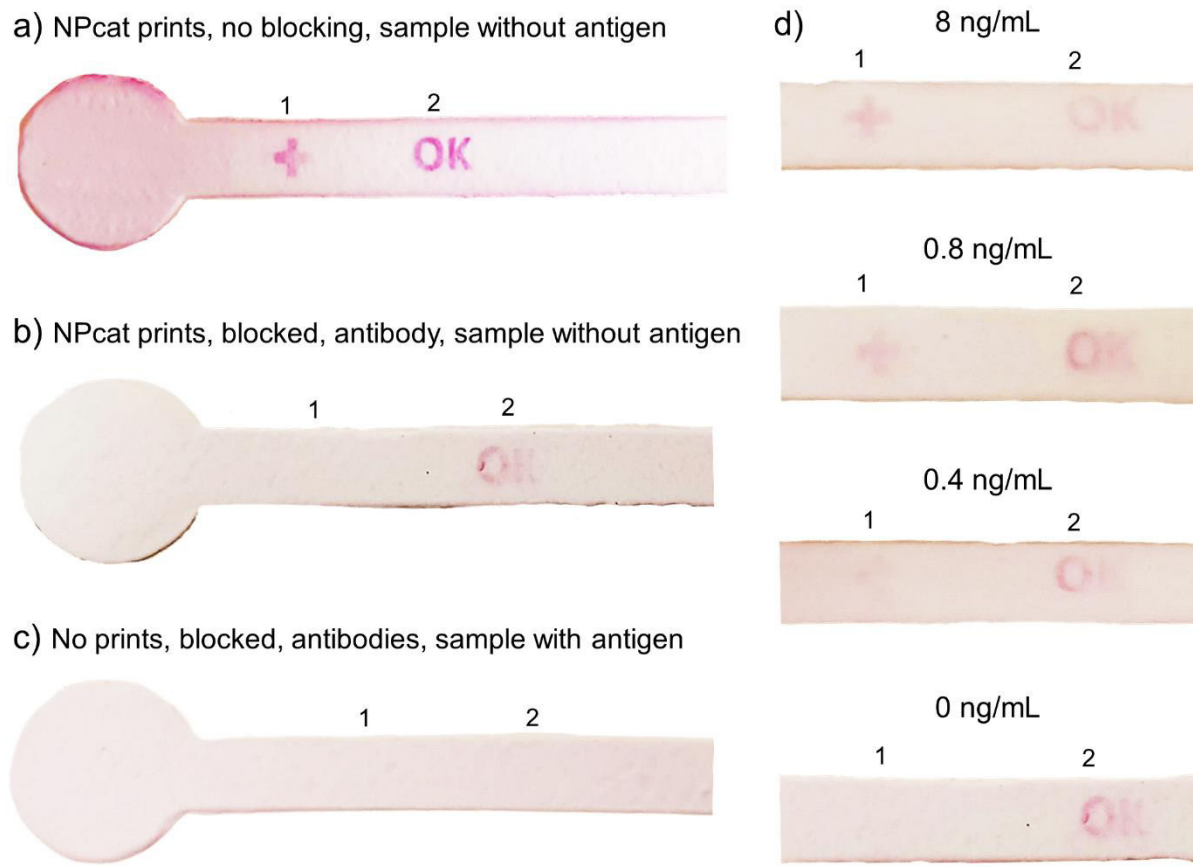


Figure 6. Effect of anchor layer, blocking treatments, and sample concentration on the performance of the immunoassay: a) A false-positive result and significant background adsorption were obtained by testing an antigen-negative sample on an untreated fluidic channel, with only printed NPcat patterns (without NPan blocking, no antibodies). b) Immunoassay prepared on the NPan-treated fluidic channel with deposited capture antibodies on the test area (“+” pattern below the marked 1, with BSA blocking) produced a clear negative result when an antigen-negative sample was tested. c) No detectable signal developed in the absence of NPcat anchor patterns after testing an antigen-positive sample (with 8 ng/mL N protein) on the NPan-blocked assay with capture (below the marked 1) and secondary (below the marked 2) antibodies. d) Testing different antigen concentrations revealed a detection limit of approx. 0.4 ng/mL, which caused a faint-colored positive sign in the test zone.

The detection limit of the developed sensor was determined. **Figure 6d** shows a gradual fading of the test pattern color with decreasing N protein concentration. The lowest detectable concentration was 0.4 ng/mL, which produced a faded “+” pattern within 5 min. To put this result in context, we note detection limits of commercial devices of 0.25⁴², 0.65⁴³, and 100⁴⁴ ng/mL obtained after 10–30 min^{42,44–46}. Moreover, the assay performance was analyzed with saliva samples and the results were compared with commercial diagnostic devices (**Figure S16**). Our developed assay performed quite effectively with human saliva. Three parallel antigen-positive samples showed three positive results and three antigen-negative samples produced three negative results. The test results were obtained in approx. 3 min. When testing the performance of commercial tests, the production of negative results was straightforward but, in some samples, it was challenging to produce distinguishable positive results. For example, Device A (**Figure S16b**) showed only one faded positive test line in 10 min (reported test time 10-20 min) or false-positive results. Specifically, Device A assays were tested with three positive samples, producing one faded positive and two false-negative results. On the other hand, Device B (**Figure S16c**) performed well and produced two clear positive results in approx. 2 min and one faded positive result in 9 min (three parallel samples, reported test time 15 min). Therefore, the performance of the developed prototype sensor is determined to be comparable or better than commercially available units.

CONCLUSIONS

We demonstrated the use of cellulose II nanoparticles to control protein interactions on surfaces. QCM-D measurements and fluorescent imaging confirmed that the nanoparticles enable a better performance compared to typical materials. Effective passivation towards non-specific proteins was obtained with NPan, while improved protein adsorption, as well as effective immobilization

of sensing antibodies, was achieved with NPcat. Additionally, NPcat was conveniently inkjet-printed on various substrates, forming patterns with high adsorption capability. Utilizing the cellulose nanospheres on patterned immunoassays enabled rapid and sensitive SARS-CoV-2 nucleocapsid detection. A detection limit of 0.4 ng/mL was measured for the developed prototype sensor, and excellent performance with saliva samples was indicated in three minutes. Considering that this sensor is an early prototype and there is a place for improvement, the cellulose II nanospheres are shown to be promising tools for enabling the development of very rapid and sensitive immunoassays.

AUTHOR INFORMATION

Corresponding Author

*E-mail: orlando.rojas@ubc.ca

Author Contributions

The manuscript was written through the contributions of all authors. All authors have approved the final version of the manuscript.

Notes

The authors declare no competing financial interest.

ASSOCIATED CONTENT

Supporting information. Additional information is provided online and includes: Schematic illustrations of the screen-printing process and the inkjet print patterns. FTIR spectra, and colloidal properties of NPan and NPcat samples. SEM images of the printed fluidic channels and their model films. AFM images of the NPan and NPcat samples on silicon wafers as well as unmodified,

NPcat- and PEI-modified model surfaces on QCM crystals. QCM-D data showing measured energy dissipation changes during adsorption of BSA and fibrinogen. QCM-D adsorption curves of anti-human IgG, BSA, and hIgG exposed pristine, NPcat- and PEI-treated model films. Confocal images showing adsorption of fluorescent-labeled antibodies on NPcat and PEI patterns on nanopapers, and on blocker-treated filter papers and printed fluidic channels. Images of prepared assays with the paper background. Test results of the commercial tests.

ACKNOWLEDGMENT

This project was funded by the European Union's Horizon 2020 research and innovation programme under grant agreement No 760876. This work was a part of the Academy of Finland's Flagship Programme under Projects No. 318890 and 318891 (Competence Center for Materials Bioeconomy, FinnCERES). KS acknowledges funding by the Aalto University School of Chemical Engineering doctoral programme. Dr. Dev Sriranganadane is acknowledged for his helpful discussion. Prof. Patrick Gane is acknowledged for his help in the development of the printed fluidic channel. We acknowledge the provision of facilities and technical support by Aalto University at OtaNano - Nanomicroscopy Center (Aalto-NMC).

REFERENCES

- (1) Carter, L. J.; Garner, L. V.; Smoot, J. W.; Li, Y.; Zhou, Q.; Saveson, C. J.; Sasso, J. M.; Gregg, A. C.; Soares, D. J.; Beskid, T. R.; Jervy, S. R.; Liu, C. Assay Techniques and Test Development for COVID-19 Diagnosis. *ACS Central Science* **2020**, *6* (5), 591–605. <https://doi.org/10.1021/acscentsci.0c00501>.
- (2) Feng, W.; Newbigging, A. M.; Le, C.; Pang, B.; Peng, H.; Cao, Y.; Wu, J.; Abbas, G.; Song, J.; Wang, D. B.; Cui, M.; Tao, J.; Tyrrell, D. L.; Zhang, X. E.; Zhang, H.; Le, X. C. Molecular Diagnosis of COVID-19: Challenges and Research Needs. *Analytical Chemistry* **2020**, *92* (15), 10196–10209. <https://doi.org/10.1021/acs.analchem.0c02060>.

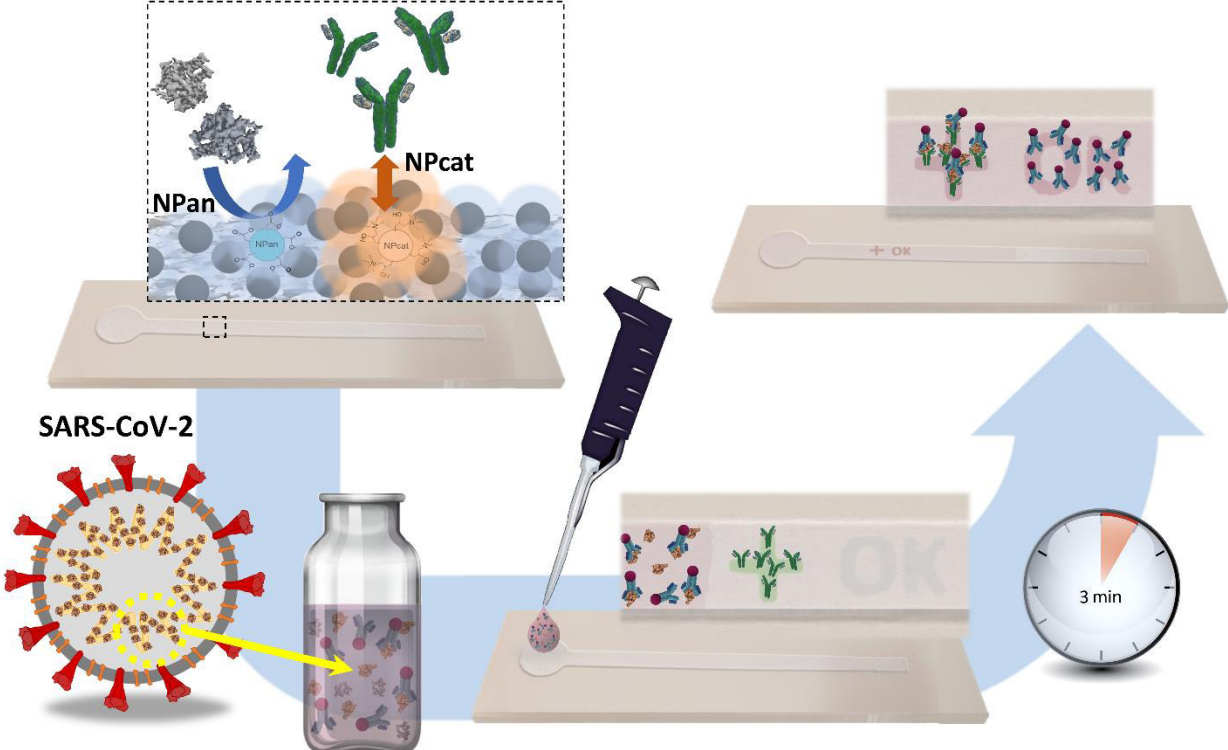
- (3) Grant, B. D.; Anderson, C. E.; Williford, J. R.; Alonzo, L. F.; Glukhova, V. A.; Boyle, D. S.; Weigl, B. H.; Nichols, K. P. SARS-CoV-2 Coronavirus Nucleocapsid Antigen-Detecting Half-Strip Lateral Flow Assay toward the Development of Point of Care Tests Using Commercially Available Reagents. *Analytical Chemistry* **2020**, *92* (16), 11305–11309. <https://doi.org/10.1021/acs.analchem.0c01975>.
- (4) SARS-CoV-2 diagnostic pipeline - FIND https://www.finddx.org/covid-19/pipeline/?section=immunoassays#diag_tab (accessed 2021-06-04).
- (5) Hristov, D.; Rijal, H.; Gomez-Marquez, J.; Hamad-Schifferli, K. Developing a Paper-Based Antigen Assay to Differentiate between Coronaviruses and SARS-CoV-2 Spike Variants. *Analytical Chemistry* **2021**, *93* (22), 7825–7832. <https://doi.org/10.1021/acs.analchem.0c05438>.
- (6) Wang, C.; Yang, X.; Gu, B.; Liu, H.; Zhou, Z.; Shi, L.; Cheng, X.; Wang, S.; Wang, C.; Gu, B.; Wang, S. Sensitive and Simultaneous Detection of SARS-CoV-2-Specific IgM/IgG Using Lateral Flow Immunoassay Based on Dual-Mode Quantum Dot Nanobeads. *Analytical Chemistry* **2020**, *92* (23), 15542–15549. <https://doi.org/10.1021/acs.analchem.0c03484>.
- (7) Chen, Z.; Zhang, Z.; Zhai, X.; Li, Y.; Lin, L.; Zhao, H.; Bian, L.; Li, P.; Yu, L.; Wu, Y.; Lin, G. Rapid and Sensitive Detection of Anti-SARS-CoV-2 IgG, Using Lanthanide-Doped Nanoparticles-Based Lateral Flow Immunoassay. *Analytical Chemistry* **2020**, *92* (10), 7226–7231. <https://doi.org/10.1021/acs.analchem.0c00784>.
- (8) Mertens, P.; de Vos, N.; Martiny, D.; Jassoy, C.; Mirazimi, A.; Cuypers, L.; van den Wijngaert, S.; Monteil, V.; Melin, P.; Stoffels, K.; Yin, N.; Mileto, D.; Delaunoy, S.; Magein, H.; Lagrou, K.; Bouzet, J.; Serrano, G.; Wautier, M.; Leclipteux, T.; van Ranst, M.; Vandenberg, O. Development and Potential Usefulness of the COVID-19 Ag Respi-Strip Diagnostic Assay in a Pandemic Context. *Frontiers in Medicine* **2020**, *7*, 225. <https://doi.org/10.3389/fmed.2020.00225>.
- (9) Taking COVID-19 Testing to a New Level | Abbott U.S. <https://www.abbott.com/BinaxNOW-Test-NAVICA-App.html> (accessed 2021 -06 -04).
- (10) FIND evaluation of SARS-CoV-2 antigen (Ag) detecting tests - FIND <https://www.finddx.org/sarscov2-eval-antigen/> (accessed 2021-06-04).
- (11) COVID-19 Ag Respi-Strip - COVID-19 Antigen rapid test <https://www.corisbio.com/products/covid19/> (accessed 2021-06-04).
- (12) SARS-CoV-2 Rapid Antigen Test <https://diagnostics.roche.com/global/en/products/params/sars-cov-2-rapid-antigen-test.html> (accessed 2021-06-04).
- (13) Sheridan, C. Fast, Portable Tests Come Online to Curb Coronavirus Pandemic. *Nature biotechnology* **2020**, *38* (5), 515–518. <https://doi.org/10.1038/d41587-020-00010-2>.

- (14) To, K. K. W.; Tsang, O. T. Y.; Leung, W. S.; Tam, A. R.; Wu, T. C.; Lung, D. C.; Yip, C. C. Y.; Cai, J. P.; Chan, J. M. C.; Chik, T. S. H.; Lau, D. P. L.; Choi, C. Y. C.; Chen, L. L.; Chan, W. M.; Chan, K. H.; Ip, J. D.; Ng, A. C. K.; Poon, R. W. S.; Luo, C. T.; Cheng, V. C. C.; Chan, J. F. W.; Hung, I. F. N.; Chen, Z.; Chen, H.; Yuen, K. Y. Temporal Profiles of Viral Load in Posterior Oropharyngeal Saliva Samples and Serum Antibody Responses during Infection by SARS-CoV-2: An Observational Cohort Study. *The Lancet Infectious Diseases* **2020**, *20* (5), 565–574. [https://doi.org/10.1016/S1473-3099\(20\)30196-1](https://doi.org/10.1016/S1473-3099(20)30196-1).
- (15) Azzi, L.; Carcano, G.; Gianfagna, F.; Grossi, P.; Gasperina, D. D.; Genoni, A.; Fasano, M.; Sessa, F.; Tettamanti, L.; Carinci, F.; Maurino, V.; Rossi, A.; Tagliabue, A.; Baj, A. Saliva Is a Reliable Tool to Detect SARS-CoV-2. *Journal of Infection* **2020**, *81* (1), e45–e50. <https://doi.org/10.1016/j.jinf.2020.04.005>.
- (16) Han, P.; Ivanovski, S. Saliva-Friend and Foe in the COVID-19 Outbreak. *Diagnostics* **2020**, *10* (5), 290. <https://doi.org/10.3390/diagnostics10050290>.
- (17) World Health Organization (WHO). *Antigen-Detection in the Diagnosis of SARS-CoV-2 Infection Using Rapid Immunoassays*; 2020.
- (18) Shen, M.; Rusling, J. F.; Dixit, C. K. Site-Selective Orientated Immobilization of Antibodies and Conjugates for Immunodiagnostics Development. *Methods* **2017**, *116*, 95–111. <https://doi.org/10.1016/j.ymeth.2016.11.010>.
- (19) Yetisen, A. K.; Akram, M. S.; Lowe, C. R. Paper-Based Microfluidic Point-of-Care Diagnostic Devices. *Lab on a Chip* **2013**, *13* (12), 2210–2251. <https://doi.org/10.1039/c3lc50169h>.
- (20) Rusmini, F.; Zhong, Z.; Feijen, J. Protein Immobilization Strategies for Protein Biochips. *Biomacromolecules* **2007**, *8* (6), 1775–1789. <https://doi.org/10.1021/bm061197b>.
- (21) Solin, K.; Beaumont, M.; Rosenfeldt, S.; Orelma, H.; Borghei, M.; Bacher, M.; Opietnik, M.; Rojas, O. J. Self-Assembly of Soft Cellulose Nanospheres into Colloidal Gel Layers with Enhanced Protein Adsorption Capability for Next-Generation Immunoassays. *Small* **2020**, 2004702. <https://doi.org/10.1002/smll.202004702>.
- (22) Beaumont, M.; Rosenfeldt, S.; Tardy, B. L.; Gusenbauer, C.; Khakalo, A.; Nonappa, Opietnik, M.; Potthast, A.; Rojas, O. J.; Rosenau, T. Soft Cellulose II Nanospheres: Sol-Gel Behaviour, Swelling and Material Synthesis. *Nanoscale* **2019**, *11* (38), 17773–17781. <https://doi.org/10.1039/c9nr05309c>.
- (23) Beaumont, M.; Rennhofer, H.; Opietnik, M.; Lichtenegger, H. C.; Potthast, A.; Rosenau, T. Nanostructured Cellulose II Gel Consisting of Spherical Particles. *ACS Sustainable Chemistry and Engineering* **2016**, *4* (8), 4424–4432. <https://doi.org/10.1021/acssuschemeng.6b01036>.
- (24) Beaumont, M.; Kondor, A.; Plappert, S.; Mitterer, C.; Opietnik, M.; Potthast, A.; Rosenau, T. Surface Properties and Porosity of Highly Porous, Nanostructured Cellulose II Particles. *Cellulose* **2017**, *24* (1). <https://doi.org/10.1007/s10570-016-1091-y>.

- (25) O'Farrell, B. Evolution in Lateral Flow–Based Immunoassay Systems. In *Lateral Flow Immunoassay*; Humana Press, 2009; pp 1–33. https://doi.org/10.1007/978-1-59745-240-3_1.
- (26) Koczula, K. M.; Gallotta, A. Lateral Flow Assays. *Essays in Biochemistry* **2016**, *60* (1), 111–120. <https://doi.org/10.1042/EBC20150012>.
- (27) Lim, H.; Turab Jafry, A.; Lee, J. Fabrication, Flow Control, and Applications of Microfluidic Paper-Based Analytical Devices. *Molecules* **2019**, *24* (16), 2869. <https://doi.org/10.3390/molecules24162869>.
- (28) Li, X.; Ballerini, D. R.; Shen, W. A Perspective on Paper-Based Microfluidics: Current Status and Future Trends. *Biomicrofluidics* **2012**, *6* (1), 11301. <https://doi.org/10.1063/1.3687398>.
- (29) Solin, K.; Borghei, M.; Imani, M.; Kämäräinen, T.; Gane, P. A. C.; Rojas, O. J. Bicomponent Cellulose Fibrils and Minerals Afford Wicking Channels Stencil-Printed on Paper for Rapid and Reliable Fluidic Platforms. *ACS Applied Polymer Materials* **2021**, Article ASAP. <https://doi.org/10.1021/acsapm.1c00856>.
- (30) Pere, J.; Tammelin, T.; Niemi, P.; Lille, M.; Virtanen, T.; Penttilä, P. A.; Ahvenainen, P.; Grönqvist, S. Production of High Solid Nanocellulose by Enzyme-Aided Fibrillation Coupled with Mild Mechanical Treatment. *ACS Sustainable Chemistry and Engineering* **2020**, *8* (51), 18853–18863. <https://doi.org/10.1021/acssuschemeng.0c05202>.
- (31) Tammelin, T.; Hippi, U.; Salminen, A. Method for the Preparation of NFC Films on Supports. Patent WO 2013/060934A2, 2013.
- (32) PowerCoat® HD - Arjowiggins Creative Papers <https://powercoatpaper.com/products/powercoat-hd/> (accessed 2020 -04 -03).
- (33) Beaumont, M.; Nypelö, T.; König, J.; Zirbs, R.; Opietnik, M.; Potthast, A.; Rosenau, T. Synthesis of Redispersible Spherical Cellulose II Nanoparticles Decorated with Carboxylate Groups. *Green Chemistry* **2016**, *18* (6), 1465–1468. <https://doi.org/10.1039/c5gc03031e>.
- (34) Sauerbrey, G. Verwendung von Schwingquarzen Zur Wägung Dünner Schichten Und Zur Mikrowägung. *Zeitschrift für Physik* **1959**, *155* (2), 206–222. <https://doi.org/10.1007/BF01337937>.
- (35) Rodahl, M.; Kasemo, B. On the Measurement of Thin Liquid Overlayers with the Quartz-Crystal Microbalance. *Sensors and Actuators, A: Physical* **1996**, *54* (1–3), 448–456. [https://doi.org/10.1016/S0924-4247\(97\)80002-7](https://doi.org/10.1016/S0924-4247(97)80002-7).
- (36) Campbell, C. T.; Kim, G. SPR Microscopy and Its Applications to High-Throughput Analyses of Biomolecular Binding Events and Their Kinetics. *Biomaterials*. 2007, pp 2380–2392. <https://doi.org/10.1016/j.biomaterials.2007.01.047>.
- (37) Vancha, A. R.; Govindaraju, S.; Parsa, K. V. L.; Jasti, M.; González-García, M.; Ballester, R. P. Use of Polyethyleneimine Polymer in Cell Culture as Attachment Factor

- and Lipofection Enhancer. *BMC Biotechnology* **2004**, *4* (1), 1–12. <https://doi.org/10.1186/1472-6750-4-23>.
- (38) Trybała, A.; Szyk-Warszyńska, L.; Warszyński, P. The Effect of Anchoring PEI Layer on the Build-up of Polyelectrolyte Multilayer Films at Homogeneous and Heterogeneous Surfaces. *Colloids and Surfaces A: Physicochemical and Engineering Aspects* **2009**, *343* (1–3), 127–132. <https://doi.org/10.1016/j.colsurfa.2009.01.039>.
- (39) Miller, A. Polyethylenimine Adhesive. US3909469A, 1974.
- (40) Kim, K. G.; Kim, S. Y. Increase in Interfacial Adhesion and Electrochemical Charge Storage Capacity of Polypyrrole on Au Electrodes Using Polyethyleneimine. *Scientific Reports* **2019**, *9* (1), 1–9. <https://doi.org/10.1038/s41598-019-38615-6>.
- (41) Hermanson, G. T. *Bioconjugate Techniques*, 2nd edition; Academic Press: New York, USA, 2008.
- (42) CorisBioConcept. *Covid19 Ag Respi-Strip*; 2020.
- (43) Grant, B. D.; Anderson, C. E.; Williford, J. R.; Alonzo, L. F.; Glukhova, V. A.; Boyle, D. S.; Weigl, B. H.; Nichols, K. P. SARS-CoV-2 Coronavirus Nucleocapsid Antigen-Detecting Half-Strip Lateral Flow Assay Toward the Development of Point of Care Tests Using Commercially Available Reagents. *Analytical Chemistry* **2020**, *92* (16), 11305–11309. <https://doi.org/10.1021/ACS.ANALCHEM.0C01975>.
- (44) Lomina. *SARS-CoV-2 N-Protein Antigen Rapid Test (Fluorescence Immunochemistry)*; 2021.
- (45) Barlev-Gross, M.; Weiss, S.; Ben-Shmuel, A.; Sittner, A.; Eden, K.; Mazuz, N.; Glinert, I.; Bar-David, E.; Puni, R.; Amit, S.; Kriger, O.; Schuster, O.; Alcalay, R.; Makdasi, E.; Epstein, E.; Noy-Porat, T.; Rosenfeld, R.; Achdout, H.; Mazor, O.; Israely, T.; Levy, H.; Mechaly, A. Spike vs Nucleocapsid SARS-CoV-2 Antigen Detection: Application in Nasopharyngeal Swab Specimens. *Analytical and Bioanalytical Chemistry* **2021**, *413* (13), 3501–3510. <https://doi.org/10.1007/S00216-021-03298-4>.
- (46) AccessBio. *Procedural Notes: CareStart COVID-19 Antigen*; 2021.

TOC IMAGE



SUPPORTING INFORMATION

Immobilized cellulose nanospheres in lateral flow immunoassay enable rapid nucleocapsid antigen-based diagnosis of SARS-CoV-2 from salivary samples

Katariina Solin^{1,2}, Marco Beaumont³, Maryam Borghei¹, Hannes Orelma², Pascal Mertens⁴, and Orlando J. Rojas^{1,5,}*

1. Department of Bioproducts and Biosystems, School of Chemical Engineering, Aalto University, Vuorimiehentie 1, FI-00076, Espoo, Finland

2. VTT Technical Research Centre of Finland Ltd., Tietotie 4E, FI-02044 Espoo, Finland

3. Department of Chemistry, Institute of Chemistry for Renewable Resources, University of Natural Resources and Life Sciences Vienna (BOKU), Konrad-Lorenz-Straße 24, A-3430 Tulln, Austria

4. Coris BioConcept, Rue Jean Sonet 4A, B-5032 Gembloux, Belgium

5. The Bioproducts Institute, Department of Chemical and Biological Engineering, Department of Chemistry and Department of Wood Science, University of British Columbia, 2360 East Mall, Vancouver, BC, V6T 1Z4 Canada

Corresponding author: Orlando J. Rojas, orlando.rojas@ubc.ca

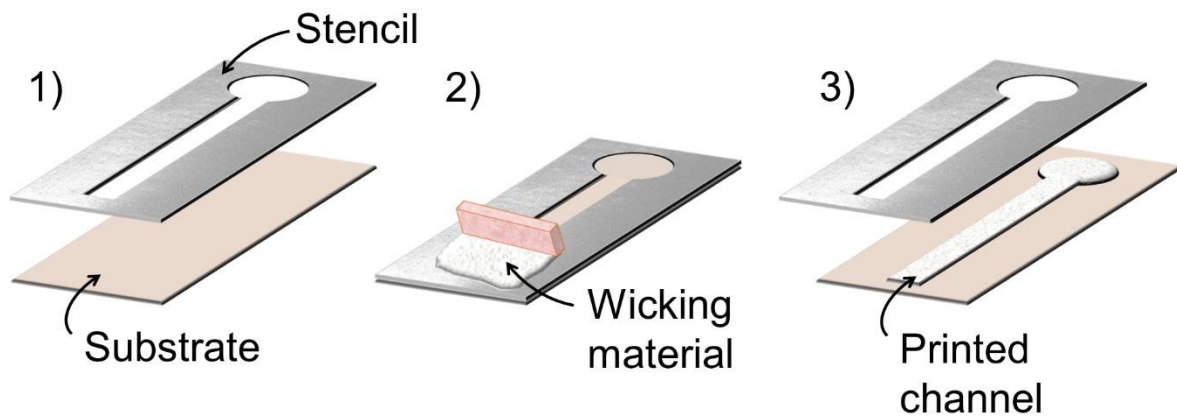


Figure S1. Schematic illustration of stencil printing of fluidic channels on paper support.

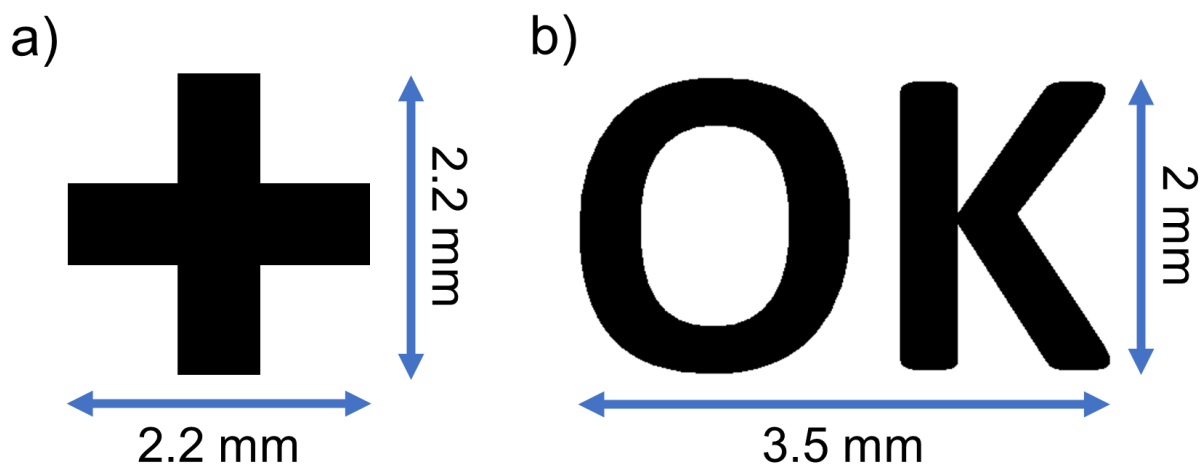


Figure S2. Printed patterns: a) Positive sign corresponds to the test line of an immunoassay and is used for the deposition of the capture antibodies (SARS-CoV-2 nucleocapsid antibody). b) “OK” sign corresponds to the control line, this pattern is either left untouched or secondary antibodies (anti-mouse IgG) are deposited on top.

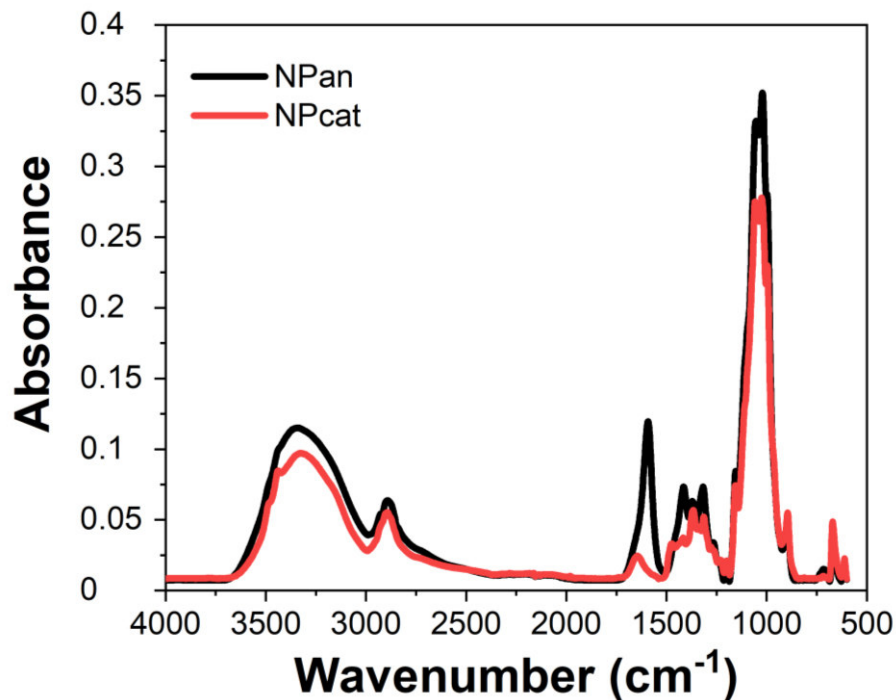


Figure S3. FTIR spectra of freeze-dried NPan and NPcat samples. The appearance of a carbonyl band (approx. 1610 cm^{-1}) in the spectrum of NPan verifies the carboxymethylation. The C-N band (approx. 1510 cm^{-1}) in the spectrum of NPcat corresponds to the introduced cationic trimethylammonium moiety proving the successful cationization.

Table S1. Colloidal properties of the NPan and NPcat (0.05 wt% in 2.5 mM NaCl buffer).

Sample	Zeta-potential (mV)	Electrophoretic mobility ($\mu\text{mcm/Vs}$)	Number-averaged particle size (nm)
NPan	-25	-1.9	65
NPcat	20	1.6	58

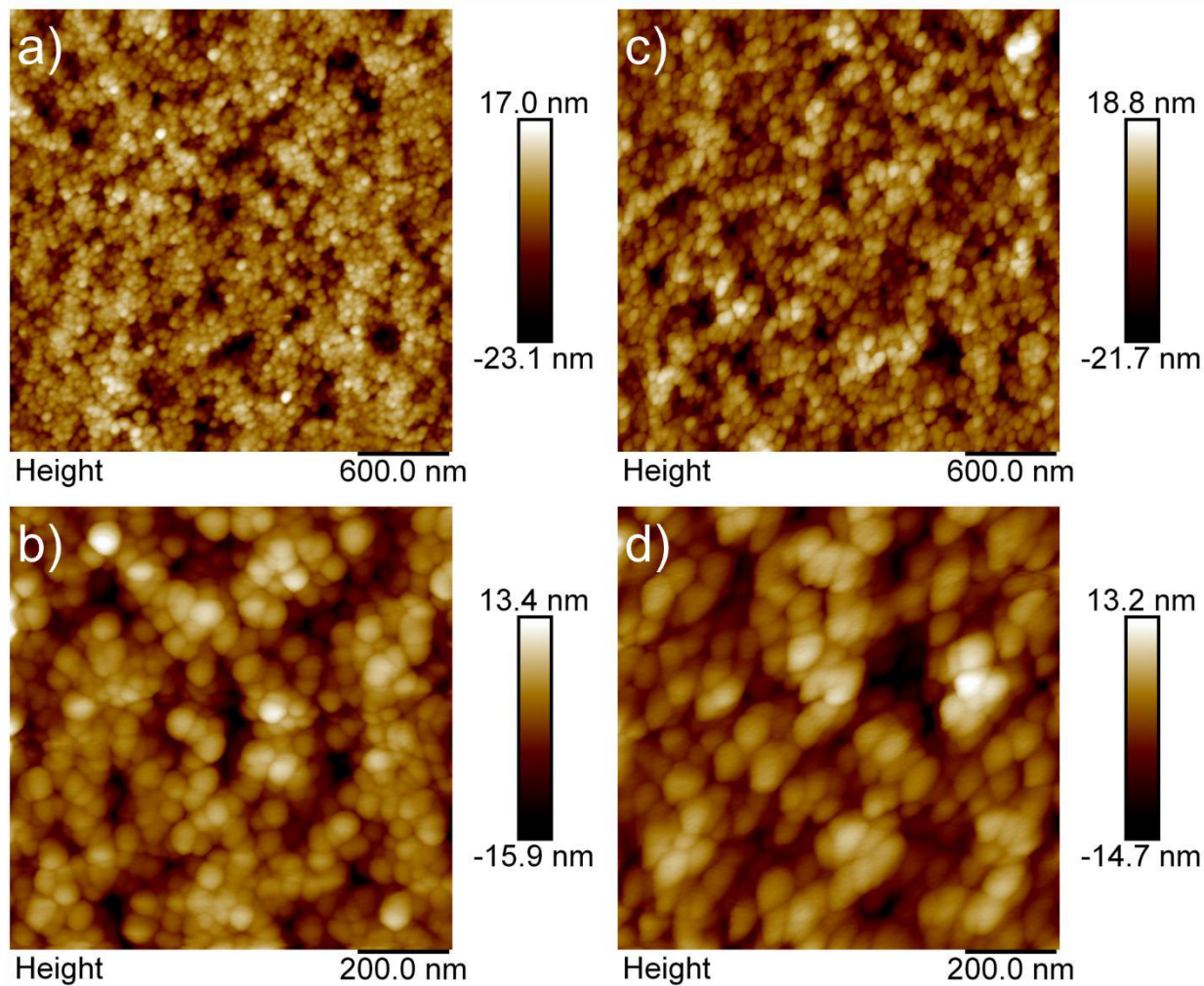


Figure S4. AFM images of a-b) NPan and c-d) NPCat films on a silicon wafer. In the NPCat images, the deformation of nanoparticles is most likely caused by the attraction of the tip and the cationic particle.

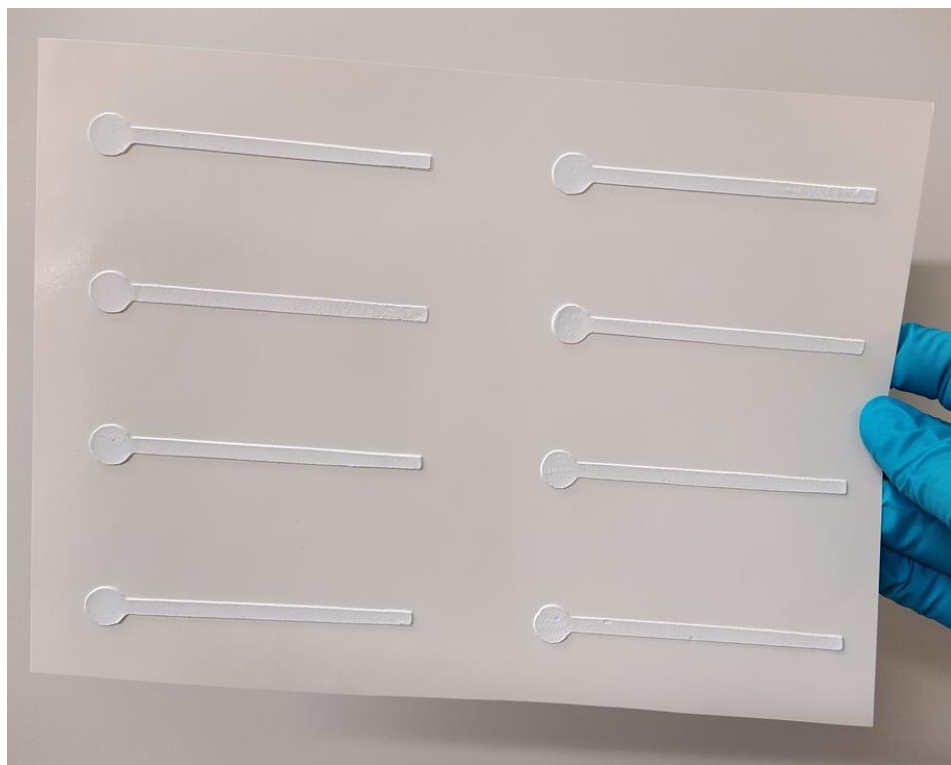


Figure S5. Printed fluidic channels on PowerCoat HD[®] paper substrate. Channels consist of an initial circular section for sample insertion and a rectangular channel for fluid transportation. These channels were used for the preparation of the immunoassays.

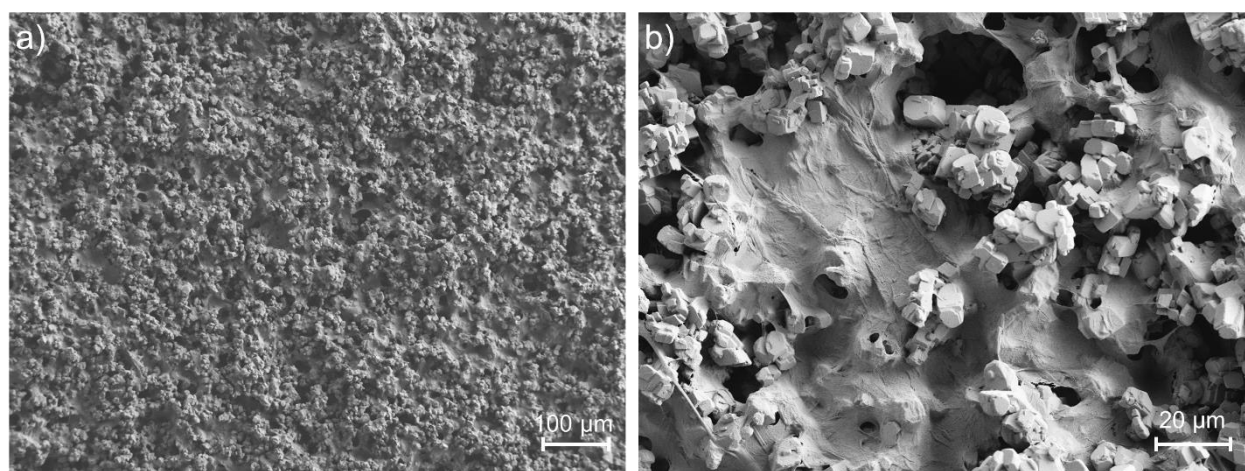


Figure S6. SEM images of the printed fluidic channels comprising CaCO₃, HefCel, CNF, and propylene glycol (Ca-CH) showing the porous surface structure: a) magnification ×100, and b) magnification ×700.

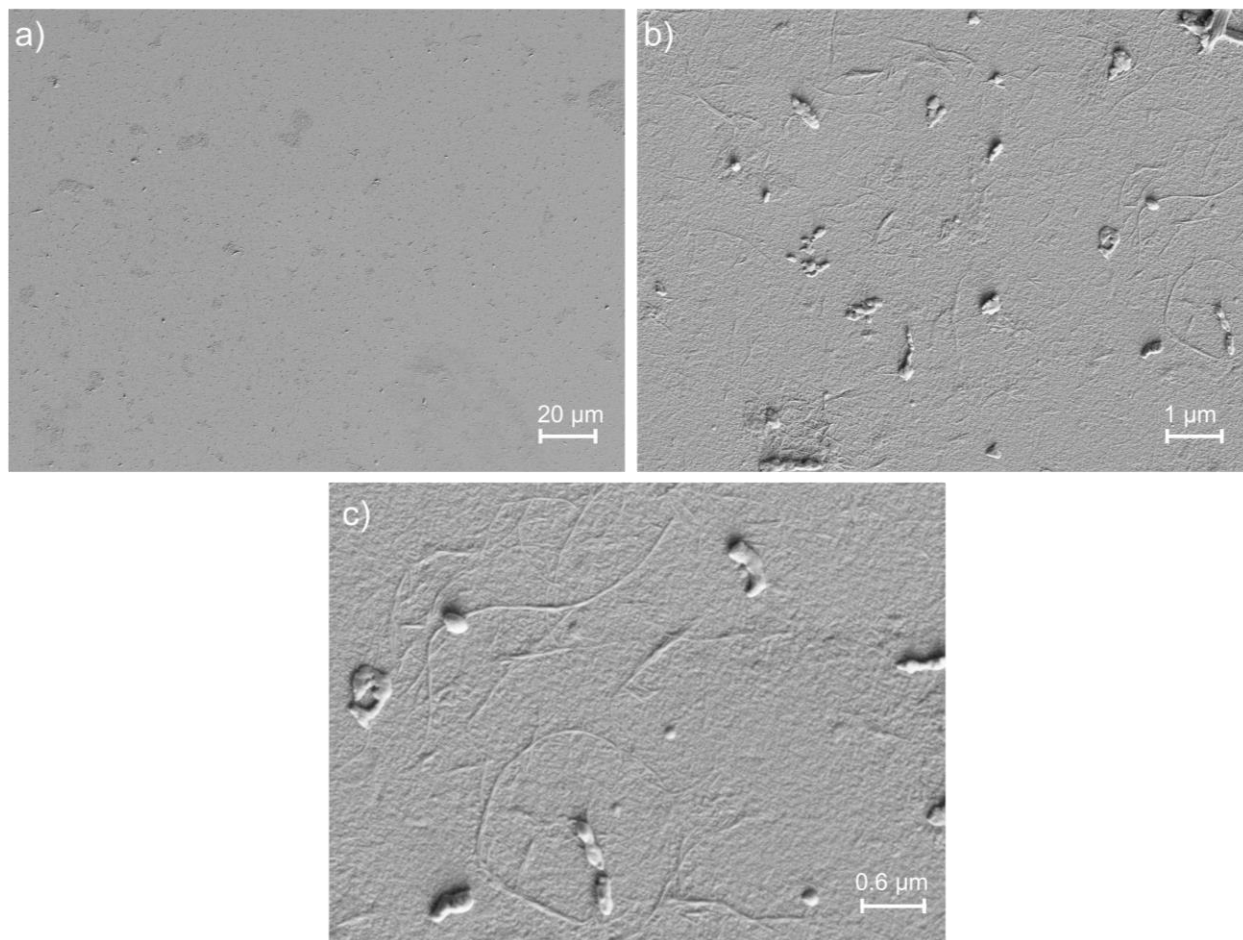


Figure S7. SEM images of the ultrathin films of the CaCH paste on QCM-D crystals: a) magnification $\times 500$, b) magnification $\times 10\,000$, and c) magnification $\times 20\,000$.

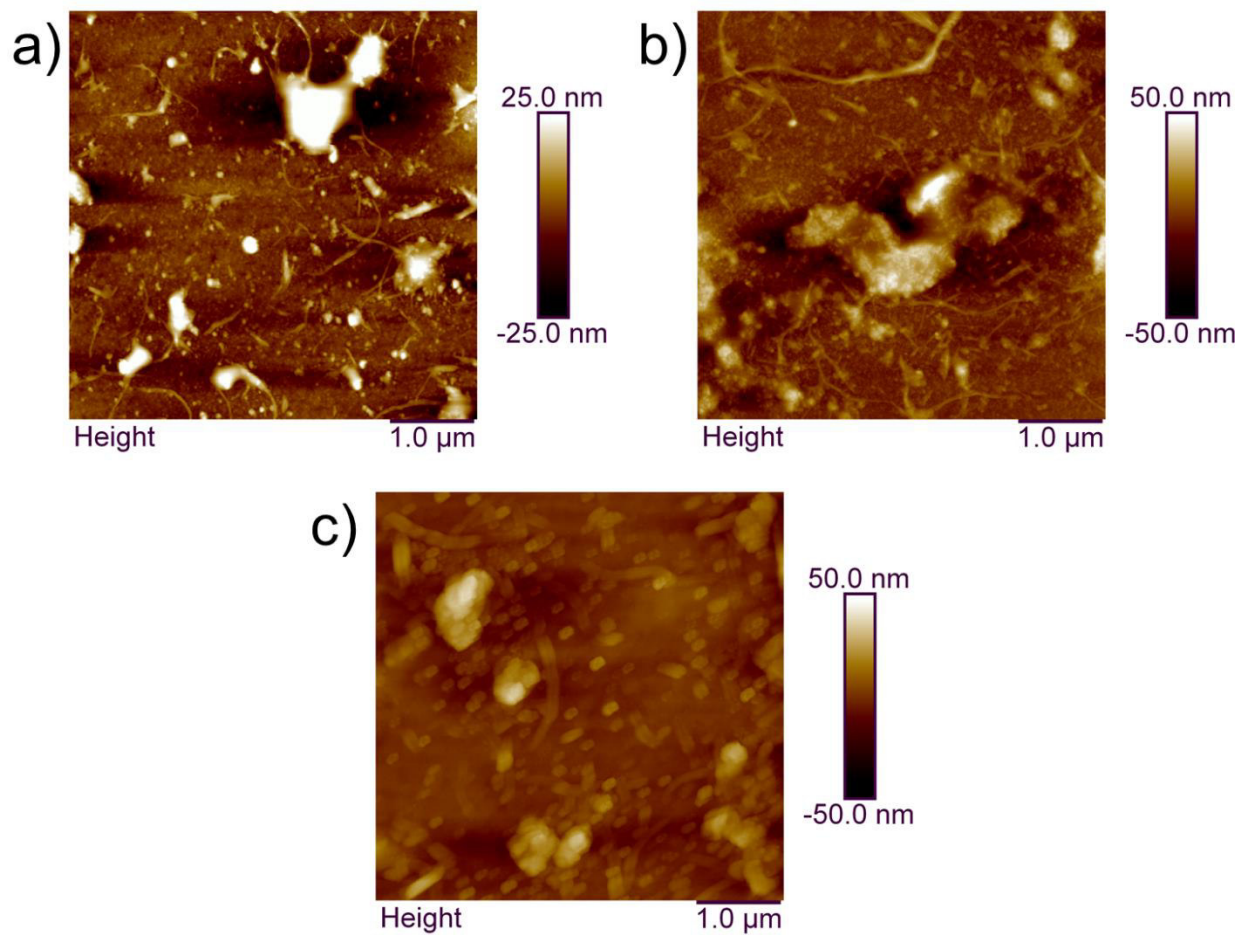


Figure S8. AFM images of the QCM-D crystals: a) unmodified model surface, b) NPcat modified model surface, and c) PEI modified model surface.

Table S2. Measured energy dissipation changes and calculated masses of the adsorbed BSA and fibrinogen on each model surface.

Adsorption of BSA			
Surface	ΔD ($\times 10^{-6}$)	Δm_{Voigt} (ng/cm^2)	$\Delta m_{\text{Sauerbrey}}$ (ng/cm^2)
Unmodified	1.5	637	576
PEI	0.6	515	571
NPcat	5.3	1345	981
NPan	-0.1	14	23.8
Adsorption of fibrinogen			
Surface	ΔD ($\times 10^{-6}$)	Δm_{Voigt} (ng/cm^2)	$\Delta m_{\text{Sauerbrey}}$ (ng/cm^2)
Unmodified	0.2	188	176
PEI	0.1	205	232
NPcat	9.5	858	896
NPan	-0.9	18	19.9
BSA	0.3	137	113

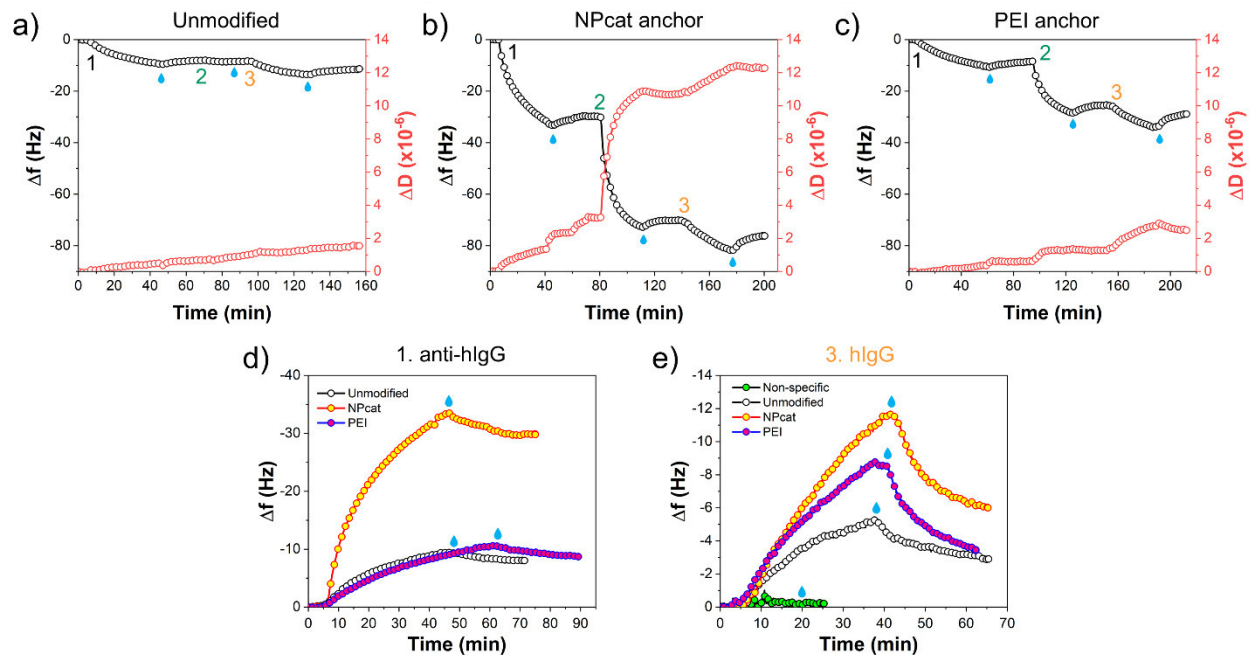


Figure S9. QCM-D data showing adsorption of anti-human IgG, BSA, and hIgG on a) unmodified model film and b) NPcat- and c) PEI-treated films. d) The effect of treatments on anti-hIgG adsorption. e) The effect of treatments on the specific adsorption of human IgG on anti-human IgG modified surfaces after BSA blocking, non-specific adsorption of hIgG on BSA-blocked model film is given as a comparison.

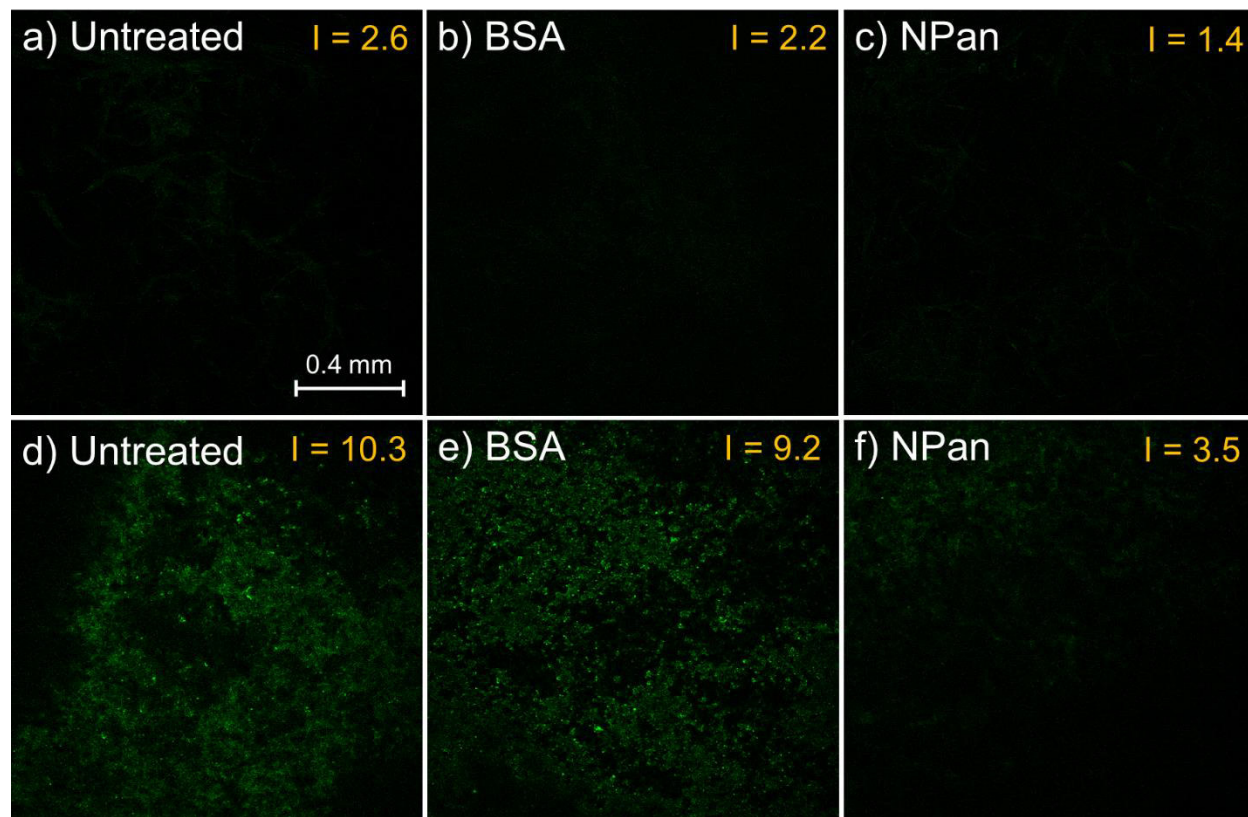


Figure S10. Confocal images of filter papers and printed fluidic channels exposed to fluorescently labeled protein (hIgG-FITC) and effect of blockers: a) unmodified filter paper, b) BSA-treated filter paper, c) NPan-treated filter paper, d) unmodified printed channel, e) BSA-treated channel and f) NPan-treated channel. The intensity of fluorescence is indicated in each sample. Images were taken with 750 V laser power.

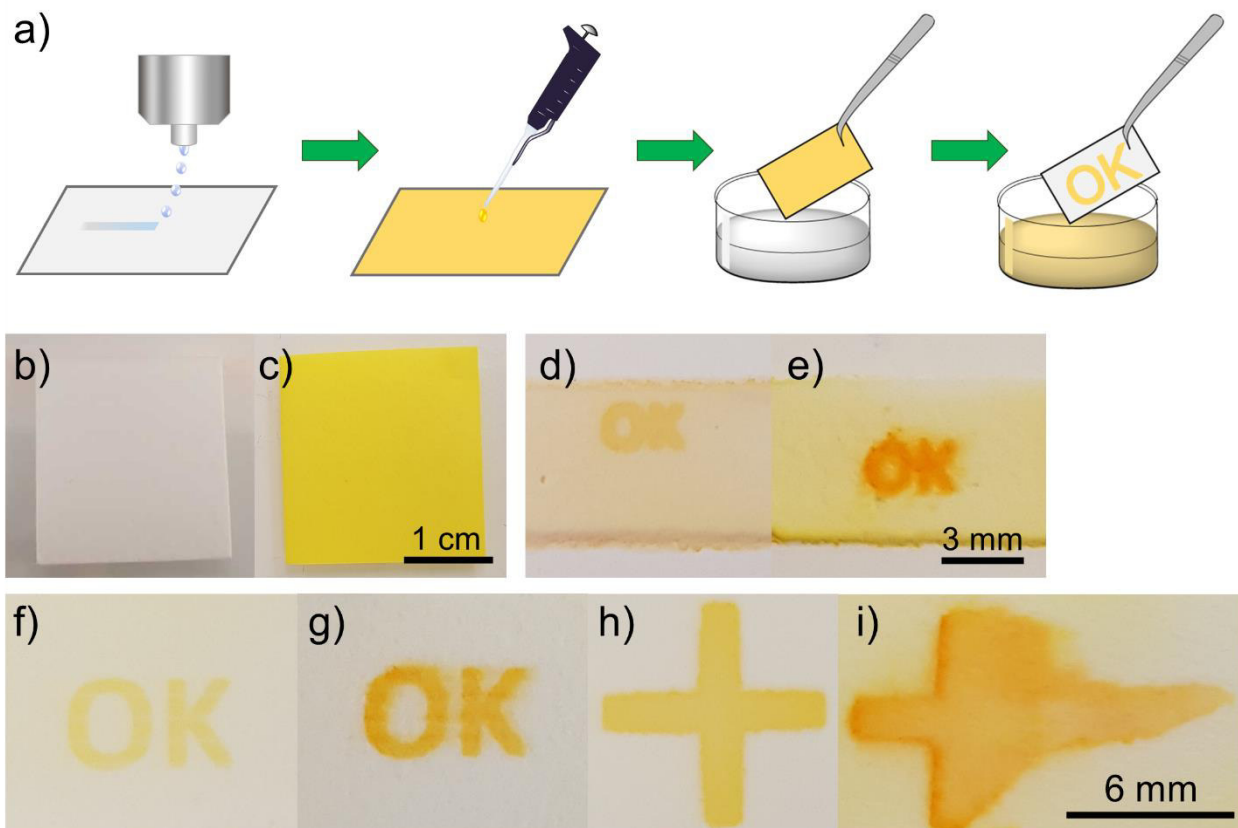


Figure S11. A *proof-of-concept* test to illustrate the immobilization capability of cationic materials demonstrated by the adsorption of a fluorescein-based dye. a) Schematic illustration of the test system: first NPcat or PEI was inkjet-printed to form a pattern on filter paper, then, the dye solution was introduced, and finally, the substrate was washed with MilliQ to reveal the patterns. Images of b) filter paper with printed NPcat pattern and b) fluorescent dyed filter paper (with the NPcat pattern). Images of the washed samples showing high adsorption capability of NPcat and PEI on the printed fluidic channel: d) NPcat pattern and c) PEI pattern (1 print layer). f-i) Images of the washed samples showing high adsorption capability of NPcat and PEI on filter paper. Patterns with one layer: f) NPcat, and g) PEI. Patterns with five layers: h) NPcat, and i) PEI. NPcat formed clear patterns with sharp edges, whereas the PEI patterns were somewhat distorted by fluid transport/flow.

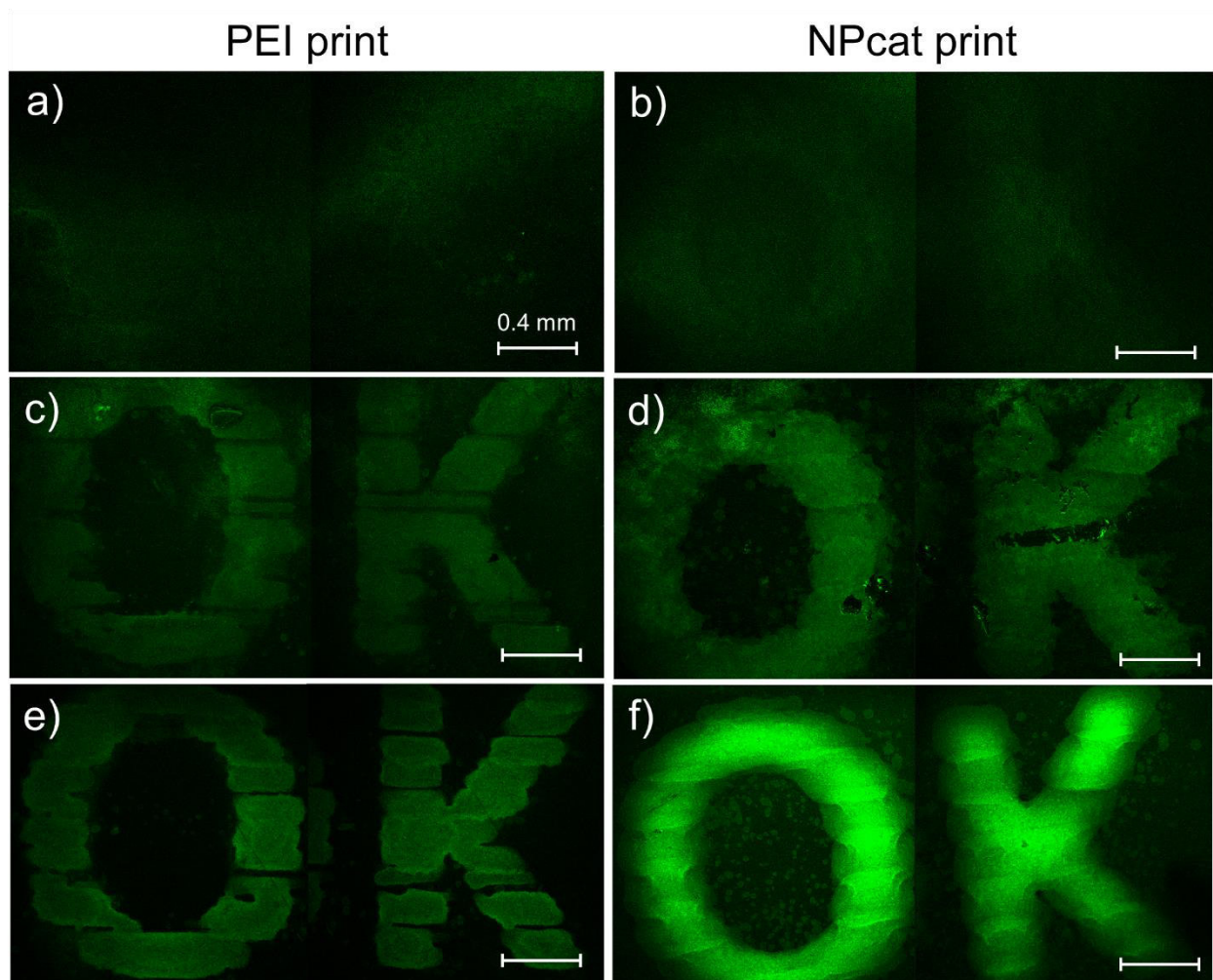


Figure S12. Confocal images of NPcat and PEI patterns printed on nanopapers showing adsorption of fluorescent-labeled proteins. a) PEI pattern (without proteins), b) NPcat pattern (without proteins), c) non-specific adsorption of hIgG-FITC on PEI pattern, d) non-specific adsorption of hIgG-FITC on NPcat pattern, e) specific adsorption of anti-hIgG-FITC on hIgG-treated PEI pattern and f) specific adsorption of anti-hIgG-FITC on hIgG-treated NPcat pattern. Images were taken with 630 V laser power.

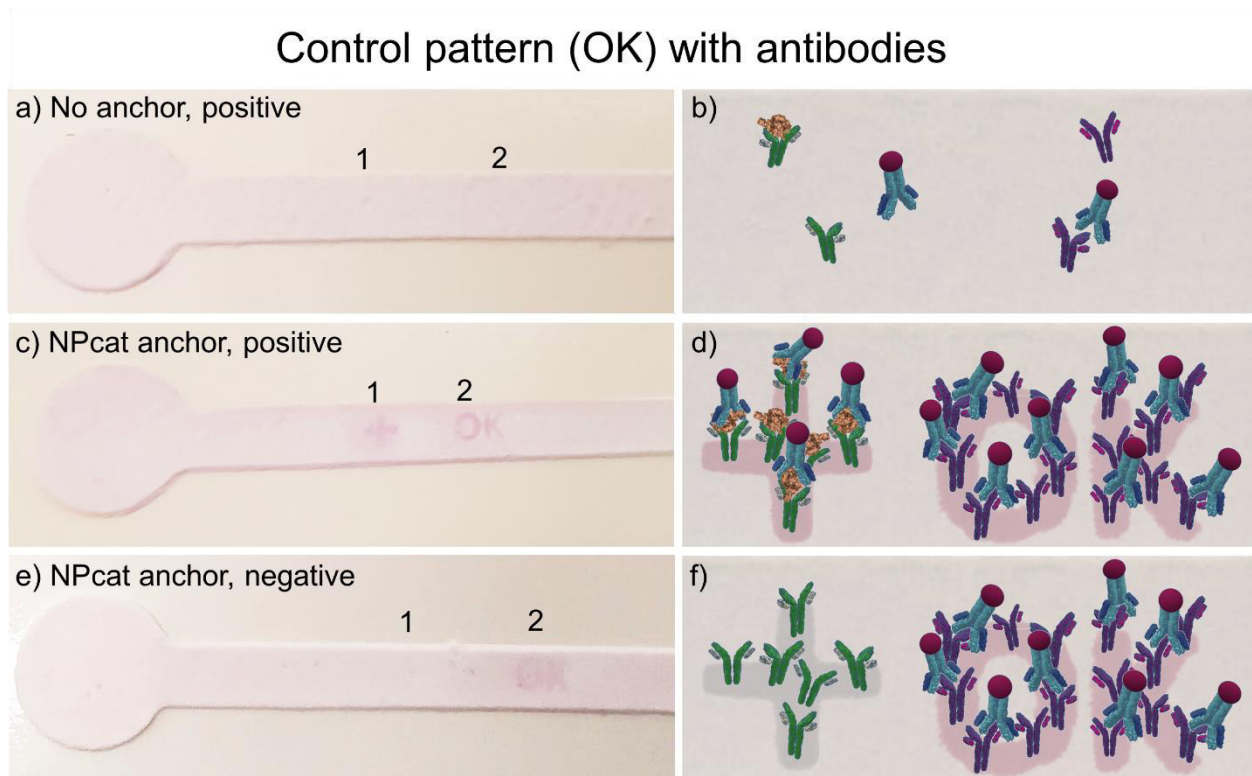


Figure S13. Effect of NPcat anchor layer on detection, antibodies on both test and control pattern. No signal was detected on assay a-b) without anchor layer (capture antibody deposited on the test area, secondary antibody deposited on control area, positive sample tested). Immobilization of the sensing elements with NPcat anchor: c) image of an assay tested with a positive sample (8 ng/mL N protein) and d) schematic illustration showing increased adsorption of detection antibody on capture antibody-nucleocapsid complex (test area) and secondary antibody (control area), e) image of channel tested with a negative sample and f) schematic illustration demonstrating adsorption of detection antibody on to the secondary antibody -covered control area.

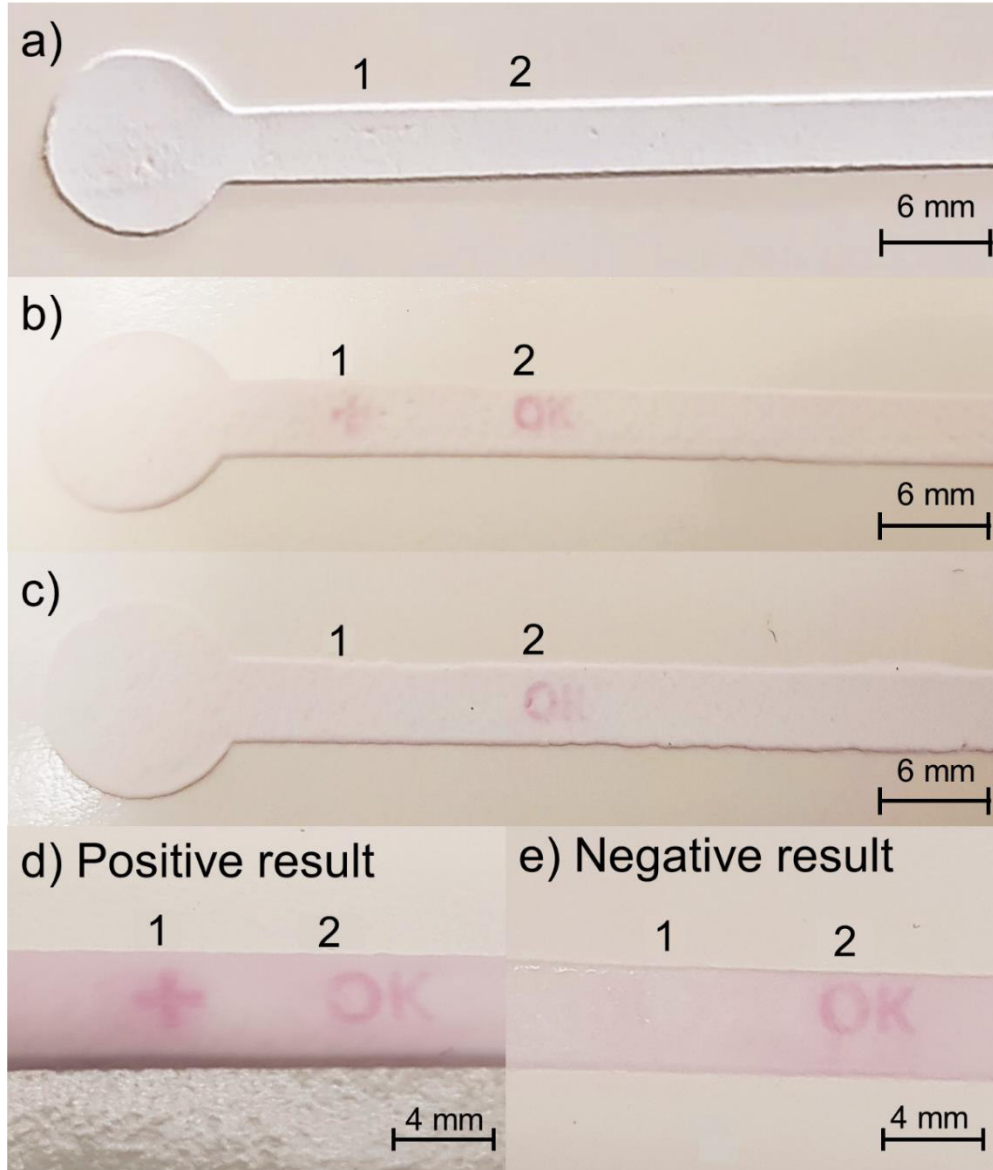


Figure S14. Images of the prepared immunoassays with paper background showing colorimetric responses before and after testing: a) untested assay with marked positions of the test (1) and control (2) areas (patterns invisible), tested and washed assays exposed to b) antigen-positive sample (8 ng/mL N protein) and c) antigen-negative sample. Corresponding color development in unwashed assays: d) antigen-positive sample and e) antigen-negative sample.

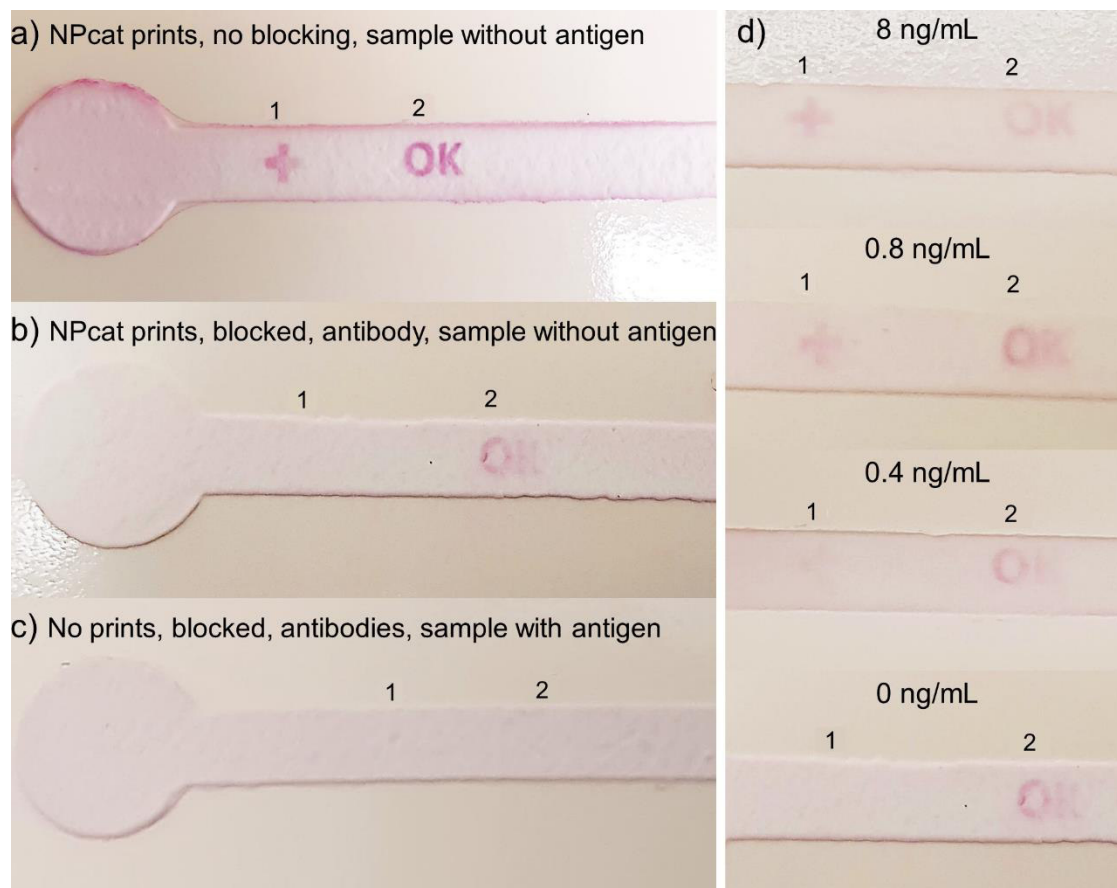


Figure S15. Images of immunoassays with and without nanoparticle treatments and with paper background: a) A false-positive result and significant background adsorption were obtained by testing an antigen-negative sample on an untreated fluidic channel, with only printed NPcat patterns (without NPan blocking, no antibodies). b) Immunoassay prepared on the NPan-treated fluidic channel with deposited capture antibodies on the test area (below the marked 1, with BSA blocking) produced a clear negative result when an antigen-negative sample was tested. c) No detectable signal developed in the absence of NPcat anchor patterns after testing an antigen-positive sample (with 8 ng/mL N protein) on the NPan-blocked assay with capture (below the marked 1) and secondary (below the marked 2) antibodies. d) Testing different antigen concentrations revealed a detection limit of approx. 0.4 ng/mL, which caused a faint-colored positive sign in the test zone.

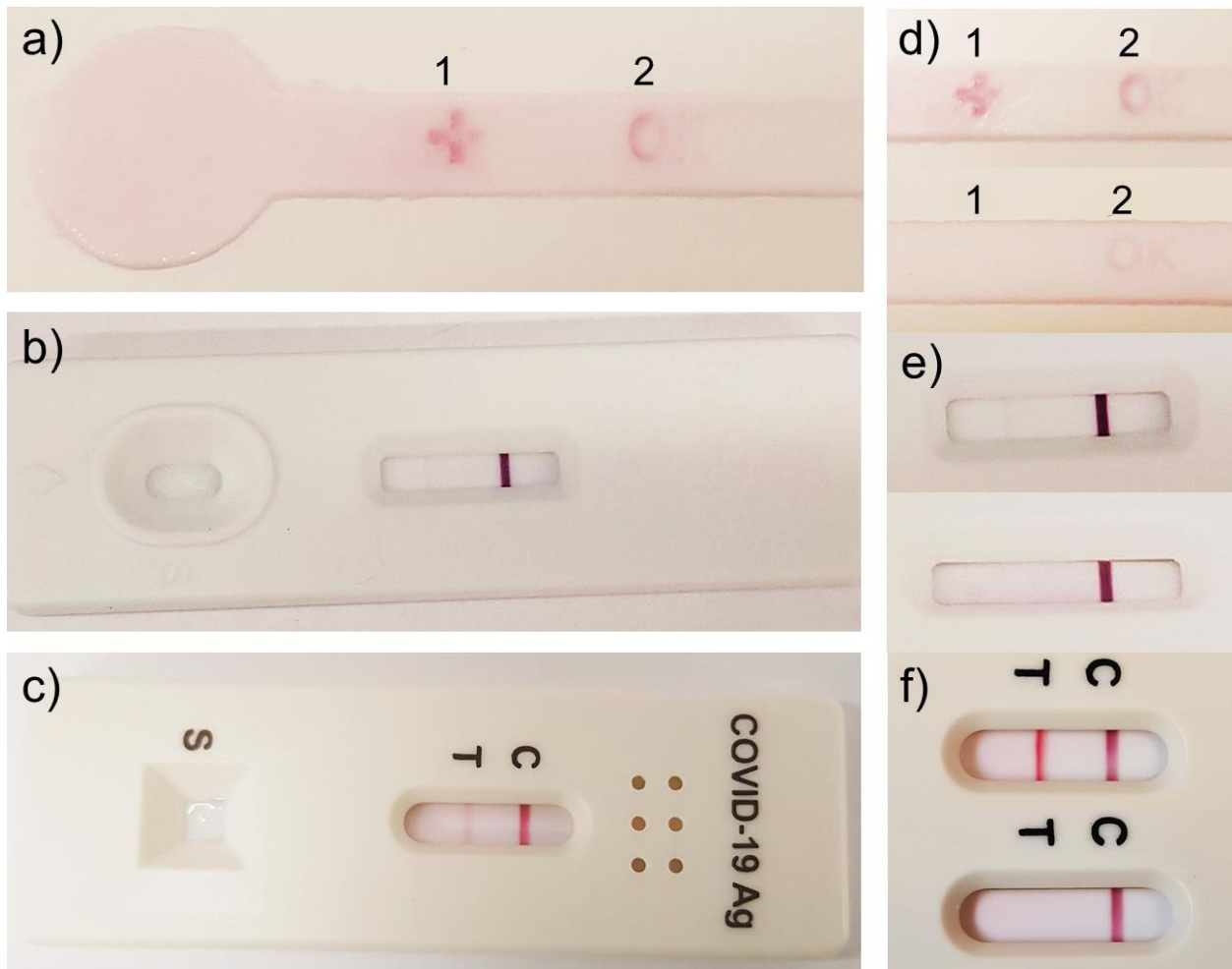


Figure S16. a-c) Testing positive saliva samples on our developed assay and comparison with commercial detection devices. The test was performed by mixing saliva and the provided buffer solution in a 1:1 ratio. To obtain a positive sample, N protein was mixed to the diluted saliva sample to gain 1 $\mu\text{g}/\text{mL}$ final concentration. Clear positive results were obtained with a) our developed assay in 3 min (three parallel samples, no washing), b) an exemplary commercial assay (Device A) showed only one faded positive test line in 10 min and lacked reproducibility (tested three times; one faded positive and two false-negative results), c) the other exemplary commercial test (Device B) produced positive results in 2-9 min (three parallel samples, the intensity of the

test line color and test time varied). Negative saliva samples were also tested and compared with the positive results: Zoomed images of the sensing areas of d) the developed assay, e) Sample A and f) Sample B tested with positive (above) and negative (below) saliva samples. Sample B and the developed assay showed good performance.